IDEA League

Master of Science in Applied Geophysics

Research Thesis

Vector and total field data inversions for magnetometer UXO surveys in the North Sea

An alternative to the industry standard

Lotte L. W. van Kerkhoven

August 5, 2022

Vector and total field data inversions for magnetometer UXO surveys in the North Sea

An alternative to the industry standard

Master of Science Thesis

for the degree of Master of Science in Applied Geophysics

by

Lotte L. W. van Kerkhoven

August 5, 2022

IDEA LEAGUE
JOINT MASTER'S IN APPLIED GEOPHYSICS

Delft University of Technology, The Netherlands
ETH Zürich, Switzerland
RWTH Aachen, Germany

Dated: *August 5, 2022*

Supervisor(s):

Evert Slob

Vsevolod Kovalenko

Peter Nieuwveld

Committee Members:

Evert Slob

Florian Wellmann

Vsevolod Kovalenko

Abstract

As an alternative to the industry standard processing of total field data, a Basin-hopping inversion can be used. Another alternative is the use of vector field magnetometers, which can be processed with a Gauss-Newton inversion. Both the Basin-hopping and Guass-Newton inversion consist of a two step inversion. First, an inversion to estimate the centre location and magnetic dipole moment of a point source is carried out, the so called point-source inversion. Second, the retrieved magnetic dipole moment can be used to reconstruct the magnetic moment with a prolate spheroid model, which is called the prolate-spheroid inversion.

First, both the TMI and vector data inversion are tested on 3000 noise-free synthetic datasets located in the North Sea where a prolate spheroid with varying shape, orientation and magnetic susceptibility creates an anomaly field. The largest global root mean square (GNRMS) error for the point-source inversion of the Gauss-Newton vector data inversion has a value in the order 10^{-9} whereas the Basin-hopping inversion for the TMI data returns for only 61% of the cases a GNRMS error in the order 10^{-7} or lower.

The result of the point-source inversion serves as a plateau for the prolate spheroid inversion; when the point-source inversion does not reach the set level of accuracy, it cannot be determined if the prolate spheroid model describes the true object well. For both the TMI and vector data, the UXO was correctly classified in 72% of the 3000 datasets.

Second, comparing the current industry standard to the Basin-hopping point-source inversion only gave inconclusive results. The estimated centre location of both methods are within a 0.15 m radius but the disagreement in magnetic moment leaves an advice on which technique would work better indecipherable.

Acknowledgements

First and foremost, I would like to thank my supervisors Evert Slob, Vsevolod Kovalenko and Peter Nieuwveld. Thank you for your valuable input, both from an academic and business perspective. I can proudly look back on a great research and a very enjoyable time too. I am looking forward to continue the work with Peter and Vsevelod for at least the coming year.

Another thanks goes out to my other dear colleagues at Fugro; to Nik Smith for giving my the tools to use Oasis Montaj, to Allessia Bortoletto for her insights on the client deliverable side and to anyone else that helped me, even if it was only a small chat during the coffee break.

Lastly, I want to thank my family and friends for all the support they have always given me. Thank you Jeffrey for listing to both my complains when something wasn't working and my rambling when I was enthusiastic when something was working. A special thanks goes out to my mom who encouraged me to follow my own path, even if it was not always the easiest one, and let me make those decisions that finally lead me to this moment, this Msc thesis.

Delft university of technology
August 5, 2022

Lotte L. W. van Kerkhoven

Table of Contents

List of Figures

List of Tables

Acronyms

TMI Total Magnetic Intensity

UXO Unexploded Ordnance

pUXO potential Unexploded Ordnance

cUXO confirmed Unexploded Ordnance

BH Basin-hopping

GN Gauss-Newton

GNRMS Global Root Mean Squared error

OM Oasis Montaj

List of symbols

Symbol	Definition	Unit
$\mathbf{E}$	Electric field	V/m
ρ	Electric charge density	C/m^3
ϵ_0	Electric permittivity in vacuum	$8.854 \cdot 10^{-12} F/m$
$\mathbf{B}$	Magnetic flux density	nT
t	Time	s
$\mathbf{J^m}$	Volumetric density of the external magnetic current	A/m^2
$\mathbf{H}$	Magnetic field	A
σ	Conductivity	S/m
$\mathbf{J^e}$	Volumetric density of the external electric current	A/m^2
μ	Magnetic permeability in vaccuum	$4\pi \cdot 10^7 H/m$
s	Time parameter in the Laplacian domain	
k	Wavenumber in Fourier domain	
$\mathbf{G}$	Forward operator: Greens tensor	
$\mathbf{r}$	Distance between the magnetic object at (x_0, y_0, z_0) and sensor (x_s, y_s, z_s) in the 3D plane	m
R	Norm of the distance vector $\mathbf{r}$	m
$\mathbf{x}$	Location in 3 dimensional space (x, y, z)	m
$\mathbf{m}$	Magnetic moment vector (m_1, m_2, m_3)	Am^2

Symbol	Definition	Unit
a	radius	m
χ	Magnetic susceptibility	
e	Stretch factor of the semi-major axis with respect to the semi-minor axes	
ϕ	Azimuth with respect to North	deg
θ	Dip angle with respect to the horizontal	deg
A	Euler rotation matrix	
$\mathbf{p}$	Model parameters	
$\mathbf{J}$	Jacobian matrix	
$\mathbf{res}$	Residual vector	
f	Function	
c	Simplification of $a^3/3 \cdot F$ Containing prolate spheroid properties e, a, χ	

Chapter 1

Introduction

Magnetometry is one of the most common survey techniques for the detection of Unexploded Ordnances (UXOs). The probability of detection of a UXO by a magnetometer survey on a controlled test site has been tested to exceed 90%, making it a reliable tool [Pederson and Stalcup, 1997]. The technique is based on the fact that most UXO's are ferromagnetic as they are made out of steel. They therefore have a magnetic susceptibility that is higher than its surrounding and create a detectable magnetic anomaly [Billings, 2004].

During World War II, the German Westwall barriers in the North Sea, also known as the Atlantic Wall, made it impossible or at least unuseful for the allied forces to conduct naval attacks. Instead, the German ships operating in that area were extensively exposed to areal explosives [Krawczyk et al., 2018]. In addition to the high contribution of dropped areal bombs, sea mines from the First and Second World War and dumped ammunition after WW II still roams the North Sea. How much ammunition is dropped in the North Sea during the two World War's is unknown, but the dumped ammunition after WW II is estimated to be at least 300.000 tons [OSPAR, 2009].

The OSPAR Commission mapped 1879 reported munitions encounters over a period from April 1999 to October 2008. Figure 1-1 shows where each UXO was found and as one can observe; a high amount was found near the Dutch coast. It is expected that still a lot of munition remains to be found.

The hazardous UXO's are however not the only objects which generate a magnetic anomaly in and below the seafloor of the North Sea. Scrap metal and other types of waste have the potential to generate magnetic anomaly fields of a similar size as UXO's. Currently, over 90% of potential UXO's (pUXO's) turns out to be false alarms, leading to high operation costs to find and examine these objects that are 90% of the cases not even hazardous.

With the plans to increase the use of sustainable energy by building several wind farms in front of the coast of the Netherlands, comes along a need for UXO surveys. Increasing the success rate of correctly labeling and accurately locating confirmed UXO's (cUXO's) is of key-importance to stay in a advantageous position in the market. But how are we going to do that?

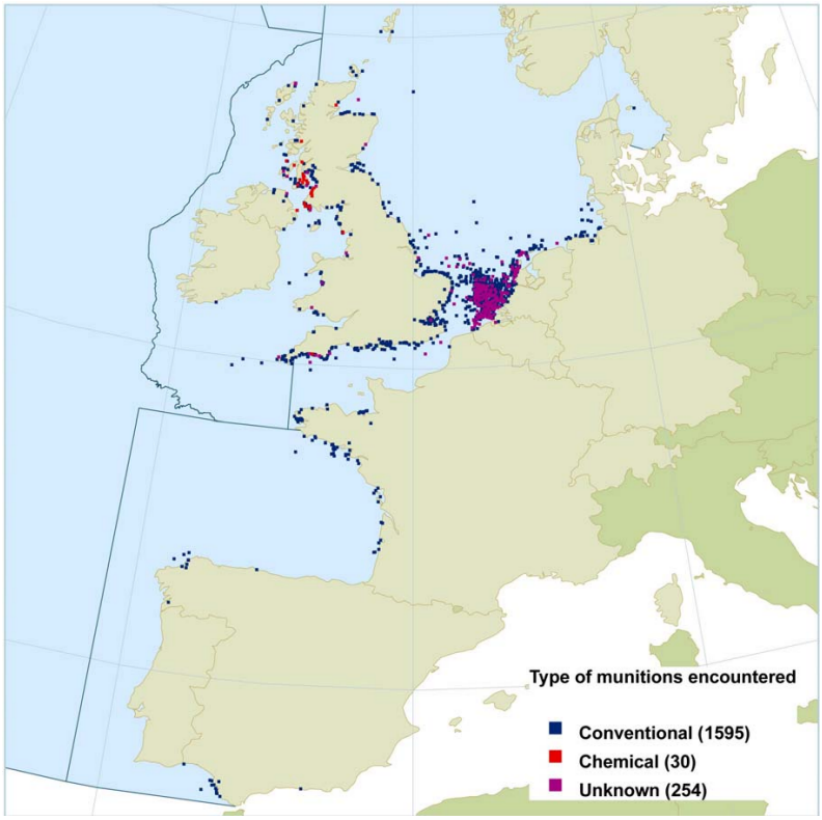

Figure 1-1: Encountered munition in the north sea between April 1999 and October 2008. Figure retrieved from [OSPAR, 2009].

1-1 Literature review

One way to decrease the number false positives is by introducing an alternative to the current industry standard data processing with Oasis Montaj. Oasis Montaj (OM) uses the Euler deconvolution to estimate the centre location and depth of the magnetic source with the aid of a structural index and the field gradients ([Thomson, 1982]; [Cooper, 2004]). Euler deconvolution models the subsurface as a set of simple sources such as monopoles and dipoles, characterised by the structural index SI.

[McPhee, 1989] also suggests modelling with a dipole point source, but rather than an Euler deconvolution, he suggest using a nonlinear least squares grid search. This inversion does not only give the centre and depth of the object, but also the magnetic moment and can even give the orientation of the dipole. Although a UXO can be approximated as being a dipole point source when the sensor is sufficiently far, taking its shape into account can give us more insight. [Altshuler, 1996] states that a UXO is a body of revolution whose asymmetry around its semi-major axis is minimal, hence it can be approached by a prolate spheroid as simplification. The main purpose of introducing the prolate spheroid model as an extent to the dipole inversion is suggested as a means to distinguish between UXO's and non-UXO's.

[Billings et al., 2002] continues on the same trend and suggests a two step inversion based on the dipole and prolate spheroid model all together; by first finding the location and magnetic

dipole moment of the object, and second, by finding the angle between the recovered dipole moment and the inducing Earth's magnetic field. The second inversion relies on the remnant magnetization to be eliminated due to shock demagnetization, such that only induced magnetization remains. When the semi-major axis of the prolate spheroid is ≤ 7 times the radius of the semi-minor axes, this angle lies within approximately 60 degrees with the Earth's magnetic field [Nelson et al., 1998].

1-2 Outline of the thesis

Literature however only talks about total field measurements or gradients of the measured total field. Recent developments in the market will make it soon possible to measure the vector field components of the magnetic field instead. In this thesis, I set up an alternative way with respect to the industry standard Oasis Montaj to process magnetometer data for UXO surveys based on [Billings et al., 2002].

This two step inversion of a dipole point source followed by a prolate spheroid inversion is tested on both synthetic TMI data as well on synthetic vector data. The dipole point source inversion for vector data uses indeed a least-squares solver, the Gauss-Newton method to be precise, but I found that the TMI needs a combination of a global and local search in the form of a Basin-hopping inversion. Alternatively to the guiding literature, the prolate spheroid inversion is not used to find the angle of the recovered dipole moment and the inducing Earth's magnetic field, but instead the orientation, shape and magnetic susceptibility of the prolate spheroid are recovered.

The thesis compares a total of three different approaches with each other. First, by looking at the synthetic TMI and vector data results from the inversion and second, by comparing the TMI inversion result to the industry standard on a real life dataset. These two examinations are used to come up with an answer to the following two reasearch questions, namely;

1. Does vector data yield better results than TMI data on synthetic data?
2. Does the two-step inversion have the potential to improve the current processing technique?

In order to answer these research questions, a firm understanding of magnetic theory and the parameters involved is necessary, which will be the topic of chapter 2. The methodology of the the inversion algorithm will be discussed in detail in chapter 3. Chapter 4 Shows the results of two datasets, where part A shows the synthetic TMI and vector datasets and part B a true dataset processed with the two different methods. These results will again be discussed in two parts in chapter 5 followed by the conclusion and an outlook to future research in chapter 6.

Chapter 2

Magnetic theory

2-1 The magnetic field

All magnetic theory start with Maxwell's electromagnetic equations [Maxwell, 1865]. This theory consists of a set of four equations, consisting of Gauss' Law, Gauss' Law for Magnetism, Faraday's Law and Ampere-Maxwell Law. The differential time-domain form of each of the laws are given in equations 2-1 to 2-4 respectively,

$$\nabla \cdot \mathbf{E} = \frac{\rho}{\epsilon_0}, \qquad (2\text{-}1) \qquad \text{[Gauss' Law]}$$

$$\nabla \cdot \mathbf{B} = \mathbf{0}, \qquad (2\text{-}2) \qquad \text{[Gauss' Law for Magnetism]}$$

$$\nabla \times \mathbf{E} + \frac{\partial \mathbf{B}}{\partial t} = -\mathbf{J}^m, \qquad (2\text{-}3) \qquad \text{[Faraday's Law]}$$

$$-\nabla \times \mathbf{H} + \sigma \mathbf{E} + \epsilon_0 \frac{\partial \mathbf{E}}{\partial t} = -\mathbf{J}^e. \qquad (2\text{-}4) \qquad \text{[Ampere-Maxell Law]}$$

Where $\mathbf{E}$ is the Electric field in V/m, ρ is the electric charge density in C/m^3, ϵ_0 is the permittivity in vacuum F/m, $\mathbf{B}$ is the magnetic flux density in nT, $\mathbf{J}^e$ and $\mathbf{J}^m$ represent the volumetric density of the external magnetic current and electrical current in A/m^2 and σ is the conductivity in S/m. Often in practice, the the Magnetic flux density $\mathbf{B}$ is used, but it can easily be linked to the magnetic field $\mathbf{H}$ according to,

$$\mathbf{B} = \mu_0 \mathbf{H}, \qquad (2\text{-}5)$$

in a homogeneous media without relaxation. In case of a heterogeneous medium with relaxation, equation 2-5 depends on location $\mathbf{x}$ and time t but will remain the property of a causal funciton.

[Blakely, 1995] uses Gauss' law for magnetism, equation 2-2, to derive a formulation for the magnetic flux density with the aid of the scalar potential. This thesis will discuss another approach which uses the Ampere-Maxwell law, equation 2-4, and Faraday's law, equation 2-3, as starting points instead.

Transforming both laws to the Laplace domain helps to get rid of the time derivatives, where $\partial/\partial t$ is transformed into the Laplacian time parameter s. Introducing $\eta(\mathbf{x}, s) = \sigma + s\epsilon$ and $\zeta(\mathbf{x}, s) = s\mu$ and translating to the Laplacian domain, denoted by the hat, results into,

$$-\nabla \times \hat{\mathbf{H}} + \eta\hat{\mathbf{E}} = -\hat{\mathbf{J}}^e, \tag{2-6}$$

$$-\nabla \times \hat{\mathbf{E}} + \zeta\hat{\mathbf{H}} = -\hat{\mathbf{J}}^m. \tag{2-7}$$

Transforming to the Laplacian domain got rid of the time derivative, the gradient however still remains. The Fourier-space transform is applied next to replace ∇ with ik. The Fourier transformed function will be denoted by the breve,

$$-i\mathbf{k} \times \breve{\mathbf{H}} + \eta\breve{\mathbf{E}} = -\breve{\mathbf{J}}^e, \tag{2-8}$$

$$-i\mathbf{k} \times \breve{\mathbf{E}} + \zeta\breve{\mathbf{H}} = -\breve{\mathbf{J}}^m. \tag{2-9}$$

Using $\eta i\mathbf{k}\cdot\breve{\mathbf{E}} = i\mathbf{k}\breve{\mathbf{J}}^e$ and $\zeta i\mathbf{k}\cdot\breve{\mathbf{H}} = i\mathbf{k}\breve{\mathbf{J}}^m$, the electric field and magnetic field can be separated into equations,

$$\breve{\mathbf{E}} = -\zeta\breve{\mathbf{A}} - \eta^{-1}\mathbf{k}(\mathbf{k}\cdot\breve{\mathbf{A}}) + i\mathbf{k} \times \breve{\mathbf{F}}, \tag{2-10}$$

$$\breve{\mathbf{H}} = -\eta\breve{\mathbf{F}} - \zeta^{-1}\mathbf{k}(\mathbf{k}\cdot\breve{\mathbf{F}}) + i\mathbf{k} \times \breve{\mathbf{A}}. \tag{2-11}$$

$\breve{\mathbf{A}}$ and $\breve{\mathbf{F}}$ represent the electric and magnetic vector potentials respectively as $\breve{\mathbf{A}} = \breve{\mathbf{G}}\breve{\mathbf{J}}^e$ and $\breve{\mathbf{F}} = \breve{\mathbf{G}}\breve{\mathbf{J}}^m$. $\breve{\mathbf{G}}$ is the Green's function which in the Laplacian-wave number domain can be represented as,

$$\breve{\mathbf{G}} = (\mathbf{k}\cdot\mathbf{k} + \zeta\eta)^{-1} = (|\mathbf{k}| + \gamma^2)^{-1}, \tag{2-12}$$

where $\gamma = \sqrt{\zeta\eta}$. Since ζ and η are constant, the only remaining variable is the wavenumber, or rather the spatial component. After separating the $\mathbf{H}$ and $\mathbf{E}$ fields, the electric field derivation stops here as we are interested only in the magnetic field. Moreover, magnetic surveys use passive sensors in a static environment where no electric field is created; we only deal with magnetostatic surveys within this thesis [Touzani and Rappaz, 2013]. η however still contains electrical components.

First off, the Green's function can be split up into four tensors, being G^{ee}, G^{em}, G^{mm} and G^{me}. The first two terms are irrelevant as they describe the relation to the **E**-field. The latter two are used to isolate the magnetic current from the electric current within the **H**-Field of the form,

$$\breve{H} = \breve{\mathbf{G}}^{me} \cdot \breve{\mathbf{J}}^{e} + \breve{\mathbf{G}}^{mm} \cdot \breve{\mathbf{J}}^{m}. \tag{2-13}$$

The First term on the right hand side can be eliminated as there is no active electric current. The only remaining factors to determine the magnetic field are thus the Greens tensor and magnetic current density. In the Fourier-Laplacian domain, $\breve{\mathbf{G}}^{mm}$ can be derived from equation 2-12 as,

$$\breve{\mathbf{G}}^{mm} = -\frac{1}{\zeta}\frac{\mathbf{kk} + \gamma^2\mathbf{I}}{|\mathbf{k}| + \gamma^2}, \tag{2-14}$$

Where $\mathbf{I}$ represents a 3×3 identiy matrix. Applying an inverse Fourier transform to go from the wavenumber domain to the space domain leads to the greens tensor in the space-Laplacian domain of the form,

$$\hat{\mathbf{G}}^{mm}(\mathbf{r}, s) = \zeta^{-1}(\nabla\nabla - \gamma^2\mathbf{I})\frac{\exp(-\gamma R)}{4\pi R} \qquad \text{for} \quad R > 0, \tag{2-15}$$

where $\mathbf{r}$ is the distance vector between the magnetic object at (x_0, y_0, z_0) and the sensor at (x_s, y_s, z_s) and R is the norm of the distance vector of $\mathbf{r}$, $R = |r|$, in metres.

The Greens function describes the behaviour of the field with respect to its location. When conducting a UXO survey, the observant, in this case the magnetometer sensors, are located outside of the source. Assuming that the distance between the sensor and the object is at least three times the largest dimension of the magnetic object, one can consider it as a magnetic dipole [Wang et al., 2020]. In this case, $\hat{\mathbf{G}}^{mm}(\mathbf{x}, s)$ takes on a specific pattern mathematical written as,

$$\hat{\mathbf{G}}^{mm}(\mathbf{r}, s) = \left[3(\hat{\mathbf{r}}\hat{\mathbf{r}} - \mathbf{I})\left(\frac{1}{R^2} + \frac{\gamma}{R}\right) + (\hat{\mathbf{r}}\hat{\mathbf{r}} - \mathbf{I})\gamma^2\right]\frac{\exp(-\gamma R)}{4\pi s\mu R} \tag{2-16}$$

where $\hat{\mathbf{r}}$ is the unit distance vector of $\mathbf{r}$, $\hat{\mathbf{r}} = \mathbf{r}/R$. Within this magnetostatic state, time is irrelevant as the magnetic field of the object will not vary over the short time-span of the survey. Moreover, γ approaches zero due to its small components inside, which simplifies equation 2-16 to,

$$\hat{\mathbf{G}}^{mm}(\mathbf{r}) = \left[3(\hat{\mathbf{r}}\hat{\mathbf{r}} - \mathbf{I})\frac{1}{R^2}\right]\frac{1}{4\pi\mu R}. \tag{2-17}$$

As equation 2-17 is not dependent on time in this magnetostatic environment, the hat on top of $\mathbf{G}$ as well as the time component gets eliminated when transforming back to the space-time domain. Rearranging then leads to,

$$\mathbf{G}(\mathbf{r}) = \frac{1}{4\pi\mu R^3}[3\hat{\mathbf{r}}\hat{\mathbf{r}} - \mathbf{I}]. \tag{2-18}$$

The 3×3 matrix $\mathbf{G}$ serves as an operator which describes how the field behaves in space, but the dipole source itself is still missing. The volumetric magnetic current density can be defined with the magnetic dipole moment m in Am^2. As the dipole is a point source and does not have a volume, $\mathbf{J}^m$ is equal to the magnetic moment. Plugging the magnetic moment and operator $\mathbf{G}$ from equation 2-18 into equation 2-13 results into the definition of the magnetic field of a dipole of the form $\mathbf{H} = \mathbf{G} \cdot \mathbf{m}$,

$$\mathbf{H}(\mathbf{r}, \mathbf{m}) = \frac{1}{4\pi\mu R^3}[3(\mathbf{m} \cdot \hat{\mathbf{r}})\hat{\mathbf{r}} - \mathbf{m}]. \tag{2-19}$$

Rather than the magnetic field, the magnetic flux density $\mathbf{B}$ is used, by applying equation 2-5 onto equation 2-19 we get,

$$\mathbf{B}(\mathbf{r}, \mathbf{m}) = \frac{1}{4\pi R^3}[3(\mathbf{m} \cdot \hat{\mathbf{r}})\hat{\mathbf{r}} - \mathbf{m}]. \tag{2-20}$$

2-2 Magnetic moment

Section 2-1 introduced us to the magnetic dipole field generated by a dipole source which has a magnetic dipole moment. The magnetic dipole moment is a 3 component vector and can be derived as being,

$$m_i = \int_V M \cdot \nabla x_i dx = \int_V M_i dx, \tag{2-21}$$

where i is an index takes on $1, 2$ or 3, M is the magnetization and V is the volume of the object. In case of constant magnetization, equation 2-21 can simply be written as $m = MV$.

A magnetic 3-Dimensional object can however be expressed with an infinite amount of poles with increasing order rather than only a single dipole [Stratton, 1941]. The magnetic dipole moment for the sake of UXO detection is hence a simplification where the monopole and higher-order poles are ignored, which will be further discussed in section 2-2-3.

The magnetic moment describes the orientation and strength of the magnetic field created by a magnetic object. It depends on the volume of the ferromagnetic object, its magnetic susceptibility and, in case of objects that are not perfectly symmetric, its orientation. Let's first look at a solid sphere as source and extend the expression for the magnetic moment to that for a spheroid.

2-2-1 Solid sphere

The magnetic dipole moment depends on the volume V of the object, which can be calculated with the aid of the radius a of the sphere as,

$$V = \frac{4}{3}\pi a^3. \tag{2-22}$$

We assume that the object is under constant magnetization, which in this case is created by the Earth's inducing magnetic field. In this case, multiplying the volume with a magnetization factor results into the magnetic moment of the sphere. How strong the magnetic moment is depends on its magnetic susceptibility χ and the inducing field $\mathbf{B}_0$ to which the object is susceptible. The magnetic moment for the solid sphere can be represented as,

$$\mathbf{m}_s = \frac{a^3 \chi \mathbf{B}_0}{3 + \chi}. \tag{2-23}$$

Equation 2-23 returns, as stated in equation 2-21, a three component vector including (m_1, m_2, m_3) in Am^2. The term 4π from the volume has been left out as it will cancel out against the 4π from equation 2-20.

A UXO however is not a perfect sphere, but more elongated, so the orientation will play a role. This means that the sphere is generally not a good approximation for the magnetic moment of the UXO.

2-2-2 Solid prolate spheroid

Following the baseline of the magnetic moment in equation 2-21, let's again start with first having a look at its shape. The prolate spheroid has 2 axes of the same length, its semi-minor axes, and one axis that is longer, the semi-major axis. In Figure 2-1, the semi-minor axes are in the y and z-direction and the semi-major axis is in the x-direction.

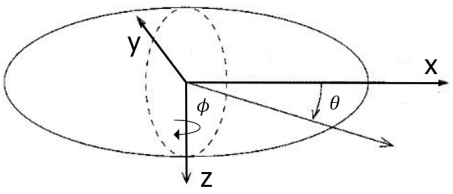

Figure 2-1: Illustration from a prolate spheroid, adaption from [Xiao and Lu, 2002]

The semi-minor axes have a radius a, whereas the semi-major axis has a radius of $e \cdot a$ where e is the so called stretch factor. When $e < 1$, the spheroid is oblate, when $e = 1$, the spheroid is a sphere and the case we will focus on is the prolate spheroid, when $e > 1$. The volume can be calculated with an updated version of 2-22 where we simply multiply with the stretch factor acording to,

$$V = \frac{4}{3}\pi e a^3. \tag{2-24}$$

Simply plugging in the prolate spheroid volume into equation 2-23 will not do the trick. As the shape is the more complex, so is the magnetization factor. The stretch factor can be found

in the form matrix F, which is a diagonal matrix with on its diagonal the form parameters in the corresponding x,y and z-directions. The form parameters $f_{i,i}$ can be calculated as,

$$F_{i,i} = \frac{1}{(\alpha_i/2+1/\chi)} \qquad \text{for} \quad i = 1, 2, 3 \ , \tag{2-25}$$

where we find again the magnetic susceptibility χ and three new parameters α_1, α_2 and α_3. These three parameters corresponds with the shape of the prolate spheroid in 3D space in the x,y,z-direction respectively. Recall that the y and z-axes are the two semi-minor axes of the object, α_2 and α_3 are equal and can be calculated as,

$$\alpha_2 = \alpha_3 = \frac{e \cdot (e + E)}{e^2 - 1}. \tag{2-26}$$

α_1 is in this system the semi-major axis and is differently calculated with,

$$\alpha_1 = -\frac{2 \cdot (1 + eE)}{e^2 - 1}. \tag{2-27}$$

Another new parameter pops up in equations 2-26 and 2-27, parameter E. E is simply a function of the stretch factor. For a prolate spheroid, the function can be written as,

$$E = \log\left[\frac{e - \sqrt{(e^2 - 1)}}{\sqrt{e^2 - 1}}\right]. \tag{2-28}$$

Radius a remains the same and has the same contribution for the magnetic moment as in equation 2-23 for the sphere.

The form matrix however represents only the case where the semi-major and semi-minor axes are completely aligned with the axes directions as defined by the inducing field $\mathbf{B}_0$. When these two coordinate systems do not align, an Euler rotation matrix should be used. Figure 2-1 shows two angles; dip angle θ between the horizontal x,y-plane and vertical z-plane, and the azimuth ϕ with respect to x in the x,y-plane. A third angle is not necessary thanks to the symmetry of the prolate spheroid in the y and z-direction. These angles are plugged in to the Euler rotation matrix A to re-orientate the spheroid to match the global orientation of the inducing field. The used Euler rotation matrix is given by,

$$\mathbf{A} = \begin{bmatrix} cos(\theta)cos(\phi) & -cos(\theta)sin(\phi) & sin(\theta) \\ sin(\phi) & cos(\phi) & 0 \\ -sin(\theta)cos(\phi) & sin(\theta)sin(\phi) & cos(\theta) \end{bmatrix}. \tag{2-29}$$

Now that all parameters are introduced, they can all be put together in the equation to calculate the magnetic moment of a prolate spheroid according to,

$$\mathbf{m}_{ps} = \frac{a^3 \mathbf{A}^T \mathbf{F} \mathbf{A} \mathbf{B}_0}{3}. \tag{2-30}$$

Note that 2-30 and 2-23 have the same result if we take the values for α_1, α_2 and α_3 to be $2/3$. In a similar fashion, parameter E in equation 2-28 can be calculated in a different matter for a oblate spheroid, when $e < 1$, namely as,

$$E = \frac{\arctan\left(2/\sqrt{1-e^2}\right) - \pi/2}{\sqrt{1-e^2}} \tag{2-31}$$

2-2-3 Multipole expansion

Even though the UXO might look like a dipole as we have assumed up till now, other poles still play their part. First and foremost, it should be stated that the monopole is neglected. Moreover, higher ranks are generally ignored as they decay rather rapidly and are therefore immeasurable. With new sensors however, it might be possible to actually measure higher poles, maybe then the multipole method, a Taylor series expansion of the poles, becomes advantageous. The multipole method starts of with the dipole moment, which was already stated before, followed by the quadrupole moment and octupole moment, according to equations 2-32 and 2-33 respectively,

$$q_{ij} = \int_V M \cdot \nabla(x_i, x_j) dx = \int_V (M_i x_j M_j x_i) dx, \tag{2-32}$$

$$o_{ijk} = \int_V M \cdot \nabla(x_i, x_j, x_k) dx, \tag{2-33}$$

which represent a rank 2 and rank 3 tensor and i, j, k are indexes with values $1, 2, 3$ [McPhee, 1989]. Each pole expansion comes along with a $1/R$ decay. Where the dipole decays with the distance cubed, for the quadrupole that is a decay of R^4 and the octupole with R^5.

Since the magnetic object we are interested in is assumed to be an ellipsoid of revolution and hence has symmetry around its semi-major axis, the quadrupole of equation 2-32 and all higher order even poles, with the exepction of the octopole, take on a value of zero [Billings, 2004]. The only remaining terms are thus the dipole, octopole and odd higher order terms. The latter is neglected aswell its field decays with $1/R^6$ at least. Combining the remaining two into one equation leads to,

$$\mathbf{B}_j = \frac{1}{R^3}\left[3\hat{r}_j\hat{r}_p m_p - m_j\right] + \frac{1}{2R^5}\left[3m^{(1)}_{jrr} - 15(\hat{r}_j\hat{r}_k m^{(1)}_{krr} + \hat{r}_k\hat{r}_r m^{(1)}_{jkr}) + 35\hat{r}_j\hat{r}_k\hat{r}_r\hat{r}_p m^{(1)}_{krp}\right]. \tag{2-34}$$

The subscripts j, k, r, p represent again the indexes which take on values of $1, 2, 3$ to match the x, y, z components. When the subscripts are repeated, the summation rule applies. Lastly, the (1) above m moreover represents that the axis of symmetry is in the x-direction.

Although worth mentioning, the octopule is ignored in the rest of this thesis. Billings2004 already stated that the octupole is too small to be measured properly and is therefore best left out. The quadrupole is r^2 less strong than the dipole, meaning that if the sensor is 4m

away from the object, the quadrupole is 16 times smaller than the dipole. That being said, with the advancing equipment I believe it should be worth examining in the future.

From now on, if the magnetic moment is mentioned this is strictly speaking the magnetic dipole moment

2-3 Earth's inducing field

The UXO does not create a magnetic field on its own, for that it needs an inducing field. In the case of passive magnetometer surveys, the inducing field is the Earth's magnetic field which was already introduced in section 2-2. The UXO creates a small perturbation, up to a maximum of a few hundred (10^2) nT in the Earth's magnetic field, which is in the order 10^4. To be able to extract information about the object from the anomaly field, it is important that the Earth's inducing magnetic field is known [Buttler, 2005].

From afar, the Earths magnetic field looks again like a dipole, similar as was stated for the Prolate spheroid, but in reality, it is far more complex than our regular spheroidal object. First, its magnetic axis is not aligned with the North and South pole of the Earth; it is approximately 10 degrees tilted with respect to the rotational axis [Courtillot et al., 1992], second, the Earth's magnetic field wanders over time and third, at the surface the magnetic field vector is far from homogeneous. The mechanics behind the magnetic field will not be discussed, but the most recent magnetic model, created by the [britisch geological survey, 2019] in October 2019, shows the heterogeneous behaviour in Figure 2-2.

The Earth's magnetic field depends on three factors: 1) the inclination, which represents the angle the magnetic field lines make with surface of the Earth, 2) the declination, which is the angle between the earth's geographic magnetic meridian, and 3) the field strength. It can be observed that indeed the inclination depends strongly on the latitude (Figure 2-2a) and the declination depends on the angle between the Earth's magnetic and geographic meridian (Figure 2-2b). The total magnetic field of the Earth however shows relatively random variations (Figure 2-2c). As the magnetic poles of the Earth wander over time, so do the inclination, declination and field strength, therefore the corrected value with respect to time are retrieved from the [national oceanic atmospheric administration US department of Commerce, ND].

To match the inducing Earth's magnetic field with the orientation of the survey plane, we follow the definition of the International Geomagnetic Reference Field (IGRF) where x is positive towards the North, y is positive towards the East and z is positive towards Earth's core. The coordinate system of the survey is rectangular, while the Earth's magnetic field is given in spherical coordinates. The change in coordinate system introduces the Earth's magnetic field as a vector with three components, B_{X0}, B_{Y0} and B_{Z0}, corresponding to the $x, y, z-$ directions of the survey location. Calculating this three component vector with the aid of the field strength T in nT, inclination I and declination D in degrees can be done as,

$$\mathbf{B_0} = \begin{bmatrix} B_{X0} \\ B_{Y0} \\ B_{Z0} \end{bmatrix} = \begin{bmatrix} T\cos(I)\cos(D) \\ T\cos(I)\sin(D) \\ T\sin(I) \end{bmatrix}. \tag{2-35}$$

The $\mathbf{B_0}$ plays a role in the magnetic moment of an object, but it is also of great importance for the measured field. Recall equation 2-20 where the anomaly field of a dipole is calculated,

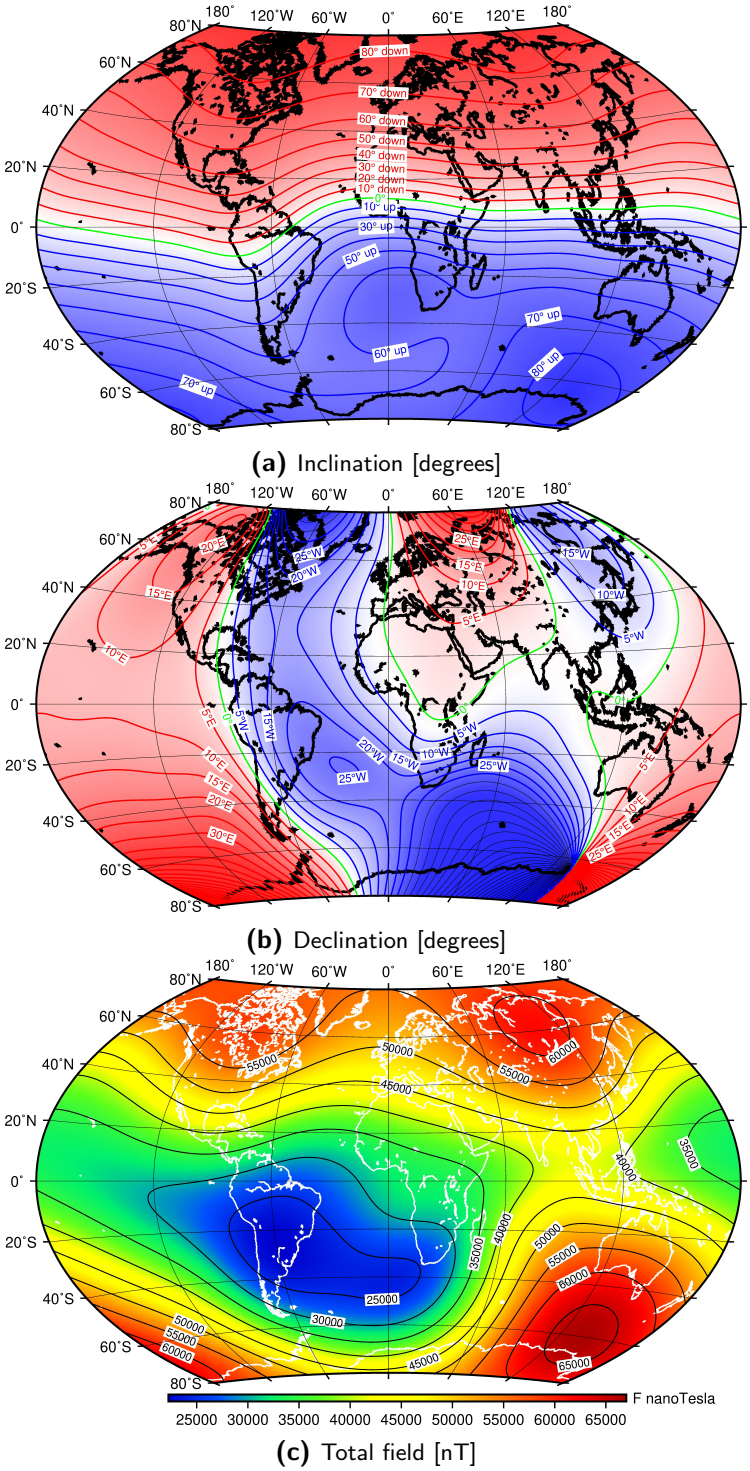

Figure 2-2: The International Geomagnetic Reference Field (IGRF) created in October 2019 for the period between 2020 and 2025 excluding its rate of change over the time period [britisch geological survey, 2019].

let's call that field $\mathbf{B_a}$. In reality, we do not simply measure $\mathbf{B_a}$; magnetometers sense both the inducing field and the anomalous field with the aid of a simple addition $\mathbf{B_a} + \mathbf{B_0}$ in the case of vector components, i.e.,

$$\mathbf{B} = \begin{bmatrix} B_{Xa} + B_{X0} \\ B_{Ya} + B_{Y0} \\ B_{Za} + B_{Z0} \end{bmatrix}. \tag{2-36}$$

The total field $|\mathbf{B}|$ is calculated by taking the norm of the vector in equation 2-36. To be consistent with equation 2-20, we also ideally want the TMI of the anomaly only. To get the TMI of the anomaly field, $|\mathbf{B}_a|$ equation 2-37 can be used,

$$|\mathbf{B}_a| = \frac{\mathbf{B}_a \cdot \mathbf{B}_0}{|\mathbf{B}_0|} \tag{2-37}$$

2-4 Parameter evaluation

All relevant parameters to construct a magnetic field created by a prolate spheroidal ferromagnetic object have been introduced. The contribution of each parameter has however not been disclosed yet, so let's do that now.

The parameters to be examined in the following sections are done so by comparing them to a default synthetic field. The synthetic field is set-up in the North Sea where the field strength is 49315.9 nT with an inclination of 67.2497 degrees and declination of 1.7592 degrees. Plugging these values into equation 2-35 leads to the Earth's magnetic field components to be,

$$\mathbf{B_0} = \begin{bmatrix} B_{X0} \\ B_{Y0} \\ B_{Z0} \end{bmatrix} = \begin{bmatrix} 19062.25 \\ 585.47 \\ 45479.07 \end{bmatrix} nT.$$

The so called "default field" is created by a large prolate spheroid with a radius of 0.30m, stretch factor of 4.0 and a susceptibility of 20. It is lying flat on the surface, meaning the dip angle is zero, and is pointing with its long axis towards North (x), meaning the azimuth is also zero. The object is located in a 3-Dimensional space at (0,0,0) while the observing sensor flies over at -1.5m. The magnetic field components of the anomaly field are shown in Figure 2-3 where the horizontal vector is spanned by $\mathbf{B}_x$ and $\mathbf{B}_y$ and $\mathbf{B}_z$ is represented in the colorscale.

The parameters to be discussed here can all be found in the magnetic moment equation for a prolate spheroid, equation 2-30, as the operator $\mathbf{G}$ in $\mathbf{B} = \mathbf{G} \cdot \mathbf{m}$ does not contain many parameters except for the location of the object. Furthermore, as the research is focused on the North Sea, a more or less constant Earth's inducing field is assumed.

The remaining parameter that will be discussed are radius a, stretch factor e, magnetic susceptibility χ, azimuth ϕ and dip angle θ.

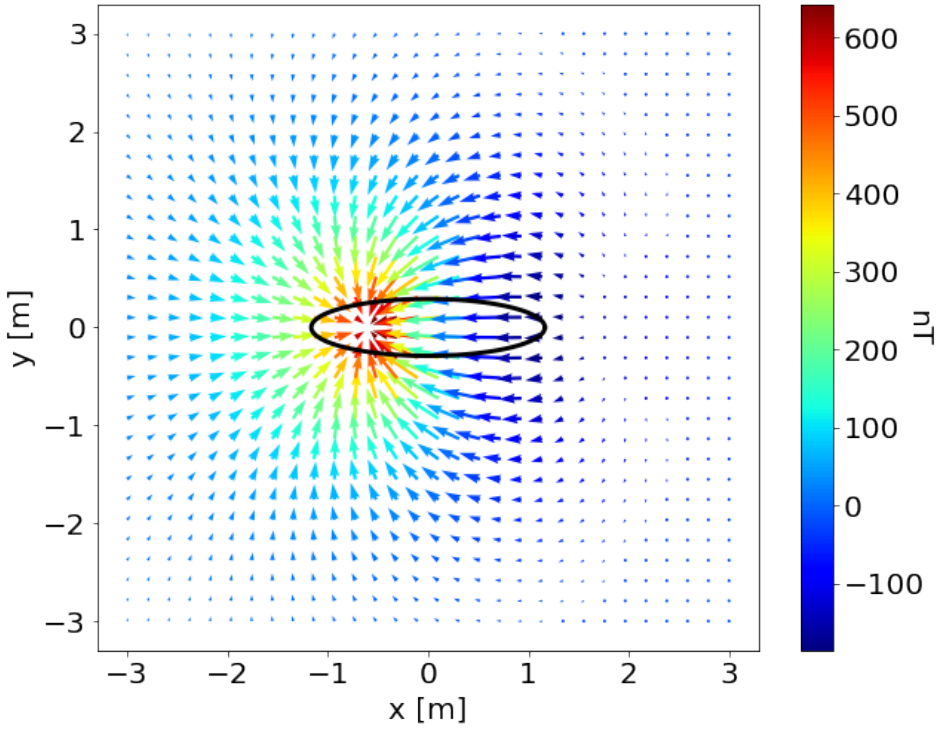

Figure 2-3: Quiver plot showing the magnetic field anomaly with a prolate spheroid of radius 0.30m, stretch factor 4.0, magnetic susceptibility 20 lying flat (dip angle of 0) with its semi-major axis pointing north (azimuth of 0). The contours of the prolate spheroid at (0,0,0) is represented with the black line.

2-4-1 Object properties

2-4-1-1 Radius

When plugging in different values for the radius, while keeping the stretch factor constant, we are simply scaling the prolate spheroid to become larger or smaller. Similarly, this scales the magnetic moment and thus the magnetic field. To put this in mathematical terms, the radius cubed is proportional to the amplitude: $a^3 \sim |\mathbf{B}|$.

The results show no significant new information but are for completeness put into Appendix A in Figure A-1.

2-4-1-2 Stretch factor

Only changing the radius while keeping all other parameters constant leads to no difference in the orientation of the field, only it's amplitude. The Stretch factor on the other hand does influence the radiation pattern. Figure 2-4 shows what happens when we decrease the stretch factor to 1 (Figure 2-4a), hence creating a sphere, and increase the stretch factor to a large value of 7 (Figure 2-4b).

The influence of derivatives on the field pattern increases with larger stretch factors; the double derivative in the x-direction determines the $\mathbf{B}_x$ pattern whereas the two horizontal

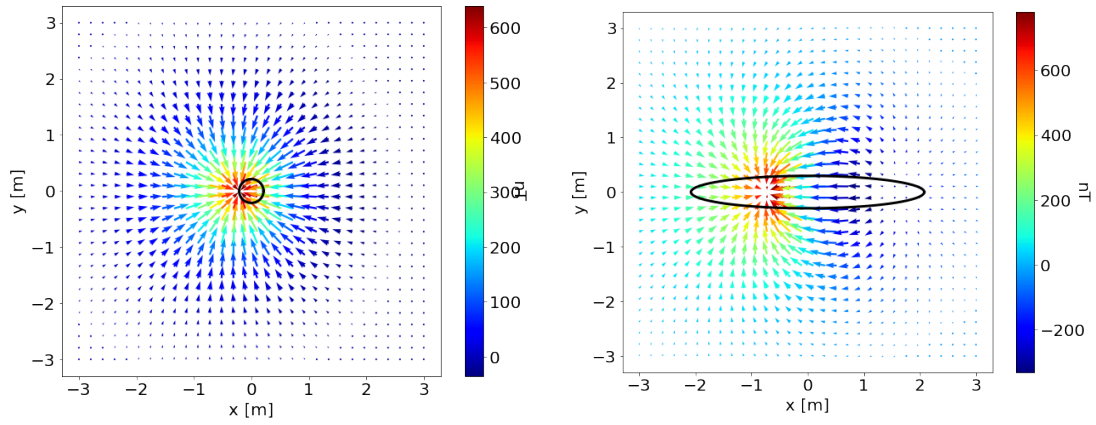

(a) $e = 1$ **(b)** $e = 7$

Figure 2-4: Setting other stretch factor values while keeping the rest the same as in Figure 2-3 shows a significant difference in field pattern.

components determine $\mathbf{B}_y$ and lastly, one derivative in the x-direction determines the B_z component.

Although the volume of the prolate spheroid in Figure 2-4b is clearly larger than the prolate spheroid from Figure 2-4a, the field strength does not increase significantly and the main variations occur in the radiation pattern.

2-4-1-3 Magnetic susceptibility

The magnetic susceptibility plays specifically at lower values a role for the amplitude of the field, which is similar to what we saw in the radius except the contribution here is lower. Also similar to the radius is that the magnetic susceptibility does not change the radiation pattern.

The scaling of χ with respect to the magnetic moment is not so simple as it is part of the denominator in the form matrix (see equation 2-25). Since the magnetic moment relates to 1χ, the effect on the amplitude of the magnetic flux density decreases as χ increases.

Again for completeness the results are portrayed in the Appendix A Figure A-2.

2-4-2 Orientation of the object

2-4-2-1 Azimuth

As the object rotates in the horizontal x,y-plane, the magnetic field pattern rotates with it to a certain extent. Since the magnetic field is induced by the magnetic field of the Earth and the anomaly field does not have the same or higher field strength as the inducing field, the orientation of the inducing field still has a leading role and the anomaly field can only deviate so much.

When the semi-major axis of the object is located in E-W direction, when $\phi = 90^o$, (Figure 2-5a), the weak B_{Y0} component causes that the field looks similar to the sphere from Figure

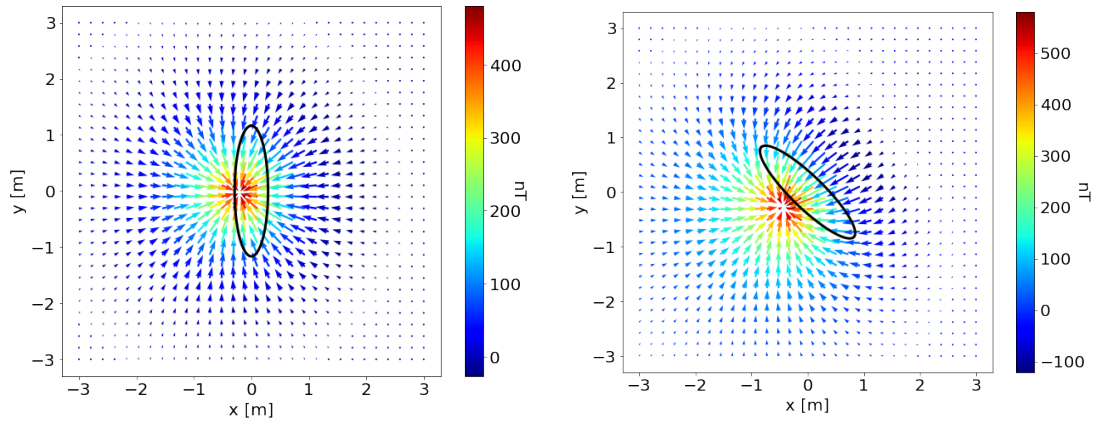

(a) $\phi = 90^o$ **(b)** $\phi = 135^o$

Figure 2-5: Setting other azimuth values while keeping the rest the same as in Figure 2-3 shows a significant difference in field pattern.

2-4a. Figure 2-5b shows an example where the object is rotated at $\phi = 135^o$ which create another shift in the pattern. The Norh-East side of the prolate spheroid shows the most significant change.

2-4-2-2 Dip angle

Lastly, there is the dip angle. Figure 2-6 shows two dip angles of 25^o and 70^o respectively. As the dip angle increases from 25^o in Figure 2-6a to 70^o in Figure 2-6b, the observed field slowly shifts to a pattern similar to the sphere from Figure 2-4a. Moreover, since the z-component of the Earth's inducing field is the strongest, the amplitude of the anomaly field increases as the semi-major axis aligns favourable with this component.

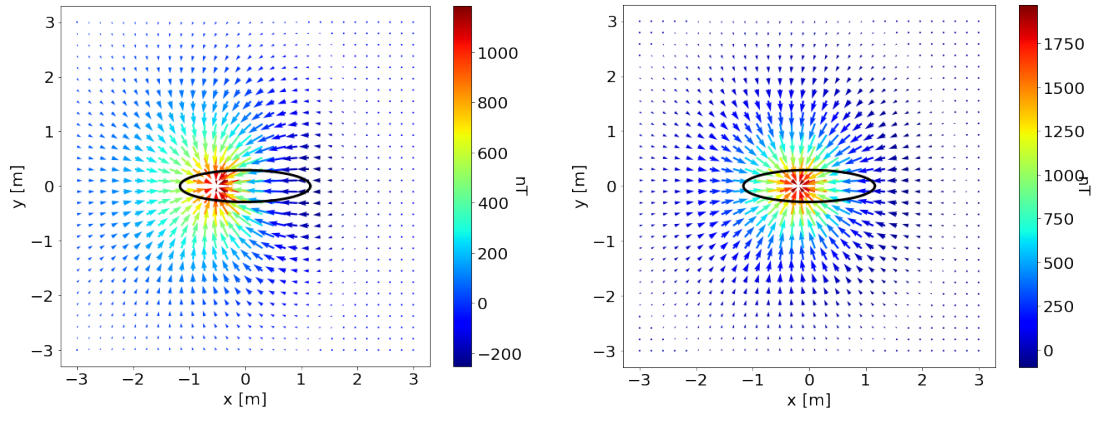

(a) $\theta = 25^o$ **(b)** $\theta = 70^o$

Figure 2-6: Setting other dip angle values while keeping the rest the same as in Figure 2-3 shows a significant difference in field pattern.

Compared to the default state in Figure 2-3, or any of the others, the dip angle shows the

largest impact on the amplitude. The stretch factor however wins when it comes to largest contribution on the field pattern.

Chapter 3

Inversion methodology

Keeping the mathematical background discussed in chapter 2 in mind, it is time to put it into practice. To obtain the main objective of the survey, i.e. find where UXO's are located, the new inversion methodology is split into two questions to solve this objective, being:

1. Can the anomaly field be modelled as coming from a point magnetic dipole?
2. If so, can the properties from this magnetic dipole be modelled as coming from a prolate spheroid instead?

Question 1 represents the first step in the inversion where the goal is to obtain the centre location and magnetic moment of the object by modelling the field as if it were to be created by a magnetic dipole. This first step in the inversion will be referred to as the point source inversion.

The second question uses the retrieved magnetic moment from the point source inversion and model it as if were to be a prolate spheroid. The prolate spheroid is used as a simplified representation of a UXO-shape. By finding the best fitting radius, stretch factor, magnetic susceptibility, azimuth and dip angle, the fit of the magnetic moment, with respect to the found magnetic moment in the point source inversion, can tell us if the object can be approximated as a prolate spheroid and hence be assumed to be an UXO. This second inversion is called the prolate spheroid inversion.

In both inversions, whether the questions can be answered with yes depends on how well the model needs to fit the true data. This chapter is subdivided into two parts according to the two inversions where first the point source inversion is discussed, followed by the prolate spheroid inversion in the second section.

3-1 Point source inversion

To select the best inversion technique, we first need to get an insight in the problem. The goal of the point source inversion is retrieving the point dipole model parameters, i.e. the centre location of the object at (x_0, y_0, z_0) and its magnetic moment (m_1, m_2, m_3), from the observed signal, e.g. B_x, B_y, B_z and/or the total magnetic intensity data.

Taken for example the most common survey set-up of 5 parallel sensors with each a sampling interval of 0.35m for surveys with a length of tens to thousands of meters, one can easily observe that there is many more than six data points per survey, consequently; there is more data than there are unknowns. Assuming this statement is the same for all survey set-ups, we are dealing with an over-determined problem with UXO magnetometer surveys.

Another thing that can be observed on top of the fact that it is over-determined, is that the problem is furthermore non-linear. Recalling from chapter 2 that the magnetic flux field is a matrix-vector product where $\mathbf{B} = \mathbf{G} \cdot \mathbf{m}$ where $\mathbf{G}$ is the operator matrix from equation 2-18 and $\mathbf{m}$ is simply the magnetic moment. The matrix-vector multiplication itself is linear, but what is non-linear is the behaviour of the location of the point source within $\mathbf{G}$.

Both TMI and vector field data are over-determined non-linear problems, but there is a slight difference in the degree of over-determinedness and non-linearity. First, the vector field data measures 3x as much data as the TMI data while using the same survey configuration, i.e. only $|\mathbf{B}|$ versus B_x, B_y, B_z. Second, as the norm of the magnetic flux field is measured in the TMI dataset, the non-linearity is not only in the $\mathbf{G}$ matrix but also in the magnetic moment vector, meaning both centre location and magnetic moment behave non-linearly.

Specifically due to this difference in degree of non-linearity between a vector field dataset and a TMI dataset, I suggest using two different inversion algorithms. The low-level of non-linearity within the vector field data makes it suitable for a Least-squares inversion such as the Gauss-Newton inversion. [Billings et al., 2002] suggested a similar method for the TMI dataset, namely an interior-reflective Newton method with trust regions. Nonetheless, due to the higher-level of non-linearity, I would suggest using a global search combined with a local search instead, such as Basin-Hopping.

Lastly, both this Gauss-Newton and Basin-Hopping algorithm can be found in the scipy optimization package for python. The scipy functions only need an objective function and initial estimate of the model parameters as bare minimum to work. There are possibilities to customise the algorithm, such as implementing boundaries on the model parameters and inserting the Jacobian matrix. Sections 3-1-1-1 and 3-1-2-1 will give an overview of the theory of the two algorithms and how it is adapted to fit with magnetometer surveys. The first estimates of both TMI and vector field inversion is the same and will be discussed in section 3-1-3, and constraining the output as discussed in section 3-1-4 is only applied on the TMI inversion.

3-1-1 Vector data inversion

3-1-1-1 Theory Gauss-Newton inversion

The Gauss-Newton method is an iterative non-linear least-squares solver which is well suited for low-level non-linear functions such as the three component B_x, B_y and B_z data. The method applies a linearization on the model function with a preliminary estimate of the unknowns with the aid of the first-order Taylor series expansion [Wang, 2012]. The second derivative is ignored as it is too computational expensive such that instead of a minimization problem, we now have a a quadratic programming problem. The method can be extended with a trust region as suggested by [Billings et al., 2002], but in this set-up phase this has been left out for now and can be reviewed later.

The objective function ψ to be optimized in the Gauss-Newton method can be written as,

$$\psi(\mathbf{p}) = \frac{1}{2}\sum_{i=1}^{n}[y_i - f_i(\mathbf{p})]^2] = \sum_{i=1}^{n} res_i(p), \tag{3-1}$$

where $\mathbf{p}$ are the model parameters, y_i is the observed signal, $f_i(\mathbf{p})$ is the analytically calculated signal based on model parameters $\mathbf{p}$ and res_i is the residual between the y and $f(\mathbf{p})$ where we sum up over each datapoint, denoted by subscript i.

The model parameters are iteratively updated until theoretically the objective function converges to its minimum. In reality however, reaching the minimum is unlikely, so a threshold will be set to define the stopping criterion; when $\psi(\mathbf{p})$ drops below a certain value or if it doesn't change for a set of consecutive iterations.

The model parameters are updated as written in equation 3-2,

$$\mathbf{p}_{k+1} = \mathbf{p}_k + \Delta\mathbf{p}_{k+1}, \tag{3-2}$$

where k stands for the iteration number; when $k = 0$, the initial estimates of the model parameters are used and updated accordingly to $k + 1$. $\Delta\mathbf{p}$ represents the step size which depends on the Jacobian matrix $\mathbf{J}$ and the residual vector $\mathbf{res}$,

$$\Delta\mathbf{p}_{k+1} = (\mathbf{J}_k^T\mathbf{J}_k)^{-1} \cdot \mathbf{J}_k^T \cdot \mathbf{res}_k. \tag{3-3}$$

The Jacobian contains as many columns as there are model parameters and as many rows as there are data points. This leads to the form,

$$\mathbf{J}_k = \begin{bmatrix} \frac{\partial}{\partial p(1)} f(x_{s(0)}, p_k) & \cdots & \frac{\partial}{\partial p(n)} f(x_{s(0)}, p_k) \\ \vdots & \ddots & \vdots \\ \frac{\partial}{\partial p(1)} f(x_{s(n)}, p_k) & \cdots & \frac{\partial}{\partial p(n)} f(x_{s(n)}, p_k) \end{bmatrix}, \tag{3-4}$$

where $p(1), ..., p(n)$ represents the model parameters and $\mathbf{x}_{s(0)}, \mathbf{x}_{s(n)}$ the location of the data point in the 3D x,y,z-plane. [Constales et al., 2017].

To summarise, the algorithm follows the following steps:

1. Fill in (first guess of) the mode parameters in $f(\mathbf{p})$.
2. Calculate the residual of $y - f(\mathbf{p})$.
3. Calculate the elements of the Jacobian matrix (equation 3-4), either with the aid of the first order Taylor series or an exact derivative if possible.
4. Update the model parameters with equation 3-3 followed by equation 3-2.
5. Repeat steps 1 to 4 until the objective function reaches a self-defined criterion.

3-1-1-2 Setting up algorithm point-source inversion for vector data

Now using the theory from section 3-1-1-1, let's apply this on the first inversion for the vector data. The model parameters in this inversion consist of the magnetic moment $\mathbf{m}$ and the centre location (x_0, y_0, z_0), which leads up to a total of six model parameters. The model parameter p is defined as,

$$\mathbf{p} = (m_1, m_2, m_3, x_0, y_0, z_0). \tag{3-5}$$

The exact derivatives with respect to each model parameter to be inserted in the Jacobian are calculated and shown in appendix B. It is important to note that the derivatives of the individual vector components B_x, B_y and B_z are not the same. TO make sure the datapoint i matches with the corresponding jacobian at entry i, the algorithm calculates residual vector and matching Jacobian matrix of each vector component of the magnetic flux field on its own and append them all together at the end according to,

$$\mathbf{res} = \begin{bmatrix} \mathbf{B}_x - f_x(x_{s(0)}, \mathbf{p}) \\ \vdots \\ \mathbf{B}_y - f_y(x_{s(0)}, \mathbf{p}) \\ \vdots \\ \mathbf{B}_z - f_z(x_{s(0)}, \mathbf{p}) \\ \vdots \end{bmatrix}, \tag{3-6}$$

where the vertical dots represent the continuation of the data column vector of $\mathbf{B}_x, \mathbf{B}_y$ and $\mathbf{B}_z$, from datapoint 0 at $\mathbf{x}_{s(0)}$ to the final datapoint N at $\mathbf{x}_{s(N)}$, and how they are appended within the residual vector. The Jacobian matrix corresponding to equation 3-6 and with model parameters $\mathbf{p}$ written out as shown in equation 3-5 is represented as,

$$J = \begin{bmatrix} \frac{\partial \mathbf{B}_x}{\partial m_1}(x_{s(0)}, \mathbf{p}) & \frac{\partial \mathbf{B}_x}{\partial m_2}(x_{s(0)}, \mathbf{p}) & \frac{\partial \mathbf{B}_x}{\partial m_3}(x_{s(0)}, \mathbf{p}) & \frac{\partial \mathbf{B}_x}{\partial x_0}(x_{s(0)}, \mathbf{p}) & \frac{\partial \mathbf{B}_x}{\partial y_0}(x_{s(0)}, \mathbf{p}) & \frac{\partial \mathbf{B}_x}{\partial z_0}(x_{s(0)}, \mathbf{p}) \\ \vdots & & & & & \vdots \\ \frac{\partial \mathbf{B}_y}{\partial m_1}(x_{s(0)}, \mathbf{p}) & \frac{\partial \mathbf{B}_y}{\partial m_2}(x_{s(0)}, \mathbf{p}) & \frac{\partial \mathbf{B}_y}{\partial m_3}(x_{s(0)}, \mathbf{p}) & \frac{\partial \mathbf{B}_y}{\partial x_0}(x_{s(0)}, \mathbf{p}) & \frac{\partial \mathbf{B}_y}{\partial y_0}(x_{s(0)}, \mathbf{p}) & \frac{\partial \mathbf{B}_y}{\partial z_0}(x_{s(0)}, \mathbf{p}) \\ \vdots & & & & & \vdots \\ \frac{\partial \mathbf{B}_z}{\partial m_1}(x_{s(0)}, \mathbf{p}) & \frac{\partial \mathbf{B}_z}{\partial m_2}(x_{s(0)}, \mathbf{p}) & \frac{\partial \mathbf{B}_z}{\partial m_3}(x_{s(0)}, \mathbf{p}) & \frac{\partial \mathbf{B}_z}{\partial x_0}(x_{s(0)}, \mathbf{p}) & \frac{\partial \mathbf{B}_z}{\partial y_0}(x_{s(0)}, \mathbf{p}) & \frac{\partial \mathbf{B}_z}{\partial z_0}(x_{s(0)}, \mathbf{p}) \\ \vdots & & & & & \vdots \end{bmatrix}, \tag{3-7}$$

For simplicity, the iteration number k of the inversion is left out in both equation 3-6 and 3-7.

Another approach could have been to group the data points together which are taken at the same location, rather than appending the vectorial components, but as long as the indexes of the Jacobian matrix and residual vector match, the order does not matter.

The build in termination criteria set-up by default in scipy are used for this inversion and uses three possible terminations, based on how much the cost function, independent variables and/or the norm of the gradient vary.

3-1-2 TMI inversion

3-1-2-1 Theory Basin-hopping inversion

Basin-Hopping combines a global and local optimization method into one algorithm [Wales and Doye, 1997]. Originally designed and optimized to find at which atom configurations the energy is minimized, it has proven itself to be versatile for many non-linear optimization problems [Olson et al., 2012].

In short, the algorithm starts off with a set of Monte-Carlo random walks with varying initial values to explore roughly where minima are located. The exploitation phase at these so called "basins", continues further with a local gradient-based optimization to find the true minima of that basin. Lastly, the found minima of the basin will be accepted or rejected based on the metropolis criterion [Iwamatsu and Okabe, 2004].

The metropolis criterion in combination with the Monte-Carlo method is also known as the Metropolis-Hastings Algorithm [Barbu and Zhu, 2020]. It only accepts moves which have a lower value for the objective function than the previous result. The objective function for the Basin-Hopping inversion is similar to the objective function of the Gauss-Newton method, equation 3-1 discussed in 3-1-1-1. However, rather than returning a residual vector, the objective function for the Basin-Hopping does not optimize the norm of the residual vector itself but this has to explicitely been given. It was here decided to use the Global Normalised Root Mean Squared (GNRMS) error,

$$GNRMS = \sqrt{\frac{\sum_i (d^i_{obs} - d^i_{est})^2}{\sum_i (d^i_{obs})^2}}, \tag{3-8}$$

where d_{obs} is the observed data and d_{est} is the reconstructed data with the aid of the results from the inversion. The field is reconstruct with equation 2-37, whereas the observed data is simply the TMI field as measured by the sensors.

The local gradient-based optimization will, similar to the Gauss-Newton method, benefit from an analytically derived Jacobian matrix for its local minima search. The derivation for the six derivatives with respect to the centre location and magnetic moment of the TMI are given again given in the appendix, Appendix B-4. Since the objective function only returns one value, the gradient only consists of one single, while still keeping its six columns to represent each derivative, note that the Jacobian remains a matrix.

The Basin-Hopping algorithm has a build in limit to the number of iterations within the local-minimizer after which it will automatically terminate. Alternatively, one can also set a threshold for the number of iterations where the outcome of the objective function remains the same for a set of function evaluations. It has been chosen to use the first option as this is by default a build-in option in the scipy package.

3-1-3 First estimates.

Both inversions have as downside that it can be sensitive to the first guesses of the model parameters, but for the GN-inversion, this plays a more significant role than for the BH inverison. Chances are that the GN inversion finds a local minimum rather than the global minimum when the initial estimates are too far off from the true values. The BH inversion prevents getting stuck with the aid of the Monte Carlo random walks, but good first estimates can still be beneficial to make sure the neighborhood near the initial model parameters is also searched.

3-1-3-1 Centre location

Let's first focus on the first guess of the centre location of the object at (x_0, y_0, z_0). [McPhee, 1989] stated that the location of the extrema of the anomaly field can give useful information on the location of the ferromagnetic object. The theory is based on the z-component of the magnetic flux field, and states that the length of the line connecting the maximum and minimum in $\mathbf{B}_z$ can be used to determine the depth of the object. Moreover, the centre of the object is located on that same line.

The latter, i.e. the location of the object in the horizontal plane, will indeed be used to determine the location of the object in the vector field inversion. For the TMI inversion however, information on the B_z field is absent, so the same technique is applied on the TMI data. For simplicity, the middle point of the line is taken as the first estimate of the horizontal centre location (x_0, y_0) in both cases.

Then for the depth of the object, the length of the line connecting the extrema of B_z varies more significantly when the object is for example rotated, indicating this method is not versatile. The same line for B_y and B_x on the other hand remains constant independent on survey or object properties. Moreover; they both are very similar in value and give a good estimate of the depth. This peak to peak distance is often an overestimation for the true

depth, therefore the length of shortest line, whether that one originates from $\mathbf{B}_x$ or $\mathbf{B}_y$, is used.

Unfortunately, the $\mathbf{B}_x$ and $\mathbf{B}_y$ field are, just like $\mathbf{B}_z$, unknown in TMI surveys. The BH inversion algorithm uses the length of the line connecting the two extrema of the TMI instead to determine z_0. An overview of the methods described above for both types of datasets is given in Table 3-1.

Table 3-1: Overview on how to find the initial estimate of the centre location.

Estimate	Vector inversion	TMI inversion
x_0, y_0	Take the middle point of the line connecting the maximum and minimum of B_z.	Take the middle point of the line connecting the maximum and minimum of the TMI
z_0	Pick the shortest distance between the maximum and minimum of either B_x or B_y	Take the distance between the maximum and minimum of the TMI

Figure 3-1 moreover serves as an example to illustrate how to get the initial estimates for the GN inversion, where the horizontal vector is spanned by $\mathbf{B}_x$ and $\mathbf{B}_y$ and $\mathbf{B}_z$ is represented on the colorscale. Note that the TMI inversion will work similarly only applying both steps on the single line connecting the two extrema of the TMI. In this example, the object is the same as in Figure 2-3; with a 0.3m radius, stretch factor of 4 magnetic susceptibility of 20 and zero azimuth and dip angle. The centre of the prolate spheroid is located at $(0, 0, 0)$ and its contour is represented in true scale. Lastly, the survey is conducted $1.5m$ above the object.

Moving on to getting the initial estimates for this example; the green line between the extrema of $\mathbf{B}_x$ has a length of $1.655m$ whereas the purple line between the extrema of $\mathbf{B}_y$ has a length of $1.448m$. Subtracting the flight height of $-1.5m$ and taking the smallest length out of the two leads to an initial estimate of $-0.0517m$. The centre location in the middle of the yellow line between the two extrema of $\mathbf{B}_z$ was picked at $(0.310, 0.0)$.

3-1-3-2 Magnetic moment

Lastly, the initial estimate for the magnetic moment does not have such easy applicable "rules of thumb" as the centre location. There are a lot of different parameters to be taken into account which can lead to hundreds Am^2 in difference in the magnetic moment. To set-up the initial estimate, we need to use some assumptions.

Before a UXO survey will take place, a desk study is done to examine which UXO's are expected to be found in the survey area. Since each type of UXO has a more or less defined radius and length, it is possible to calculate the maximum and minimum value of each individual component of the magnetic moment vector. Taken the same object, the extrema of the the magnetic moment depend on orientation, but the extrema for each of the three magnetic moment components (m_1, m_2, m_3) do not occur at the same orientation. Hence, to get the absolute maximum and minimum of each component, they are all three calculated separately using those different angles.

We benefit here from the fact that in some cases the magnetic moment in one direction is maximized due to an alignment with the Earth's inducing field. This means that the

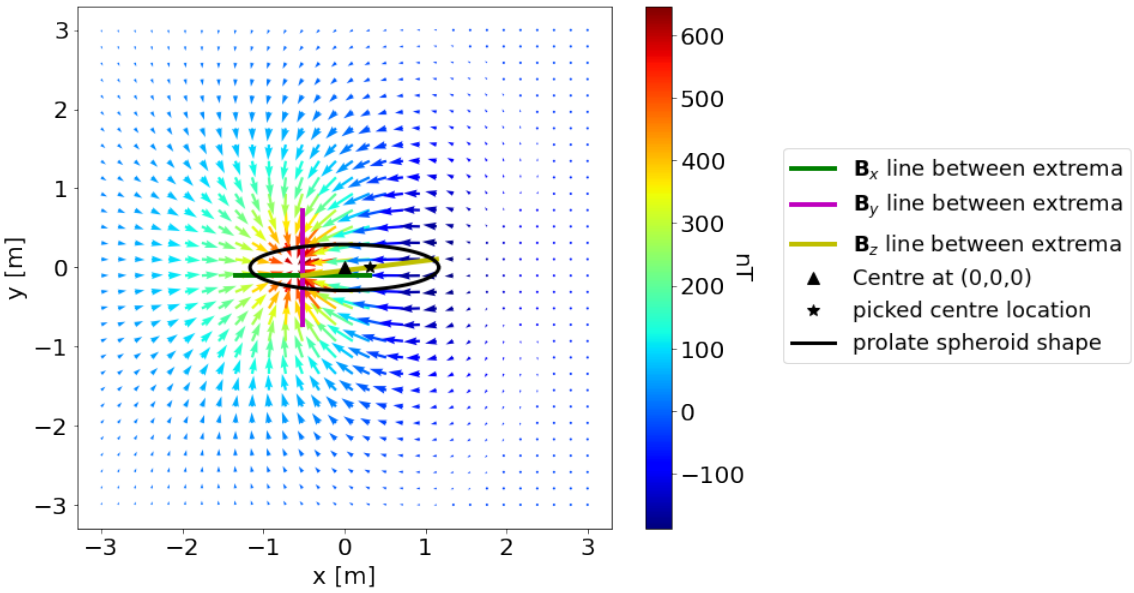

Figure 3-1: Quiver plot of $\mathbf{B}_x, \mathbf{B}_y$ and $\mathbf{B}_z$. The green and purple lines connect the extrema of $\mathbf{B}_x$ and $\mathbf{B}_y$ respectively, which can be used to determine z_0. The middle of the green line, conecting the extrema of $\mathbf{B}_z$, is used as an initial estimate of the horizontal location. The object generating the magnetic field anomaly is a prolate spheorid and the contour of its true shape and size are represented. It is located at the triangle at $(0, 0, 0)$ and the survey was conducted at a height of $-1.5m$

orientation to get these extrema depends on the inclination and declination of the Earth's magnetic field. Assuming the object is a prolate spheroid which can be reconstructed with equation 2-30, the parameters necessary to calculate the individual extrema of m_1, m_2 and m_3 are given in Table 3-2. Aside from the orientation, the table moreover shows that in case of multiple UXO's, the radius, stretch factor and susceptibility for the minimum value of m_3 needs to be picked carefully. Lastly, not enough proof of a good relationship was found in some cases, in those cases, the angle is given for a field of inclination 67.2497 degrees and a declination of 1.7592 degrees.

The initial estimate is calculated by taking the mean value from the individual calculated maximum and minimum value of m_1, m_2 and m_3 as calculated by the values from Table 3-2.

3-1-4 Constraining outputs.

It is possible for both the Gauss-Newton inversion as well as the Basin-hopping inversion to apply boundaries on the model parameters output. Opposite to the first estimates, the BH inversion in this case benefits significantly from setting boundaries, preferably as small as possible such that the Monte Carlo random walks don't wander to far away. The constraints can also be applied on the GN inversion, but this results into minor or no improvements.

Constraining the magnetic moment is rather difficult as a wide range of values naturally occur for UXO's. One constraint that could potentially be applied is to limit m_3 to only positive values, but this will not yield a better result or faster inversion.

Table 3-2: An overview on the orientations needed to calculate the maximum and minimum values of m_1, m_2 and m_3 individually. In case of multiple UXO's in the area, the table specifies moreover if the largest object into account or a smaller one should be taken into account, ditto for the magnetic susceptibility.
* *The relation between the inclination or declination was not found in this case. The orientation is based on a field with an inclination of 67.2497 degrees and a declination of 1.7592 degrees*

Magnetic moment	Parameter	Max expected value	Min expected value
m_1	ϕ	between 0 and -10	90 at +/− 0 declination, 90 elsewhere
	θ	inclination/2	90-inclination/2
	e, a, χ	maximum	maximum
m_2	ϕ	135*	70*
	θ	0	40*
	e, a, χ	maximum	maximum
m_3	ϕ	0	0 - declination
	θ	45 + inclination/2	45 - inclination/2
	e, a, χ	maximum	max e, min χ & a

Limiting the minimum search with respect to the model parameters of the centre location (x_0, y_0, z_0) is a lot easier and thus recommendable. Setting the boundaries for the horizontal components x_0 and y_0 is strongly dataset dependent, it is important to keep in mind that it is better to make the bounds too large than too small. The vertical component z_0 on the other hand is a lot easier to constrain. The estimated depth with the aid of the distance between the two extrema is usually an overestimation of the true depth of the object, meaning it will return a value that the magnetic object is further away than it actual is. It can therefore be used as an upper bound according to our coordinate where z is positive downwards system. The seafloor can be used as the lower bound. To play it safe, it is however recommendable to stretch both bounds by a little bit.

3-2 Prolate spheroid inversion

After successfully running the point source inversion, the next step is to perform the prolate spheroid inversion to check if we are indeed dealing with a prolate spheroidal-like shaped object. This inversion uses the magnetic moment retrieved from the previous point source inversion to determine the size of the object, assuming it would have a prolate spheroidal shape. These properties include, referring back to equation 2-30, the radius and stretch factor. To get these however, the orientation, dip angle θ and azimuth ϕ, as well as the magnetic susceptibility of the object first needs to be determined. This prolate spheroid inversion on itself hence also contains two separate inversion steps.

3-2-1 Inversion for dip angle and azimuth

To retrieve the azimuth ϕ and dip angle θ, it is possible to solve a system of equations and see which combination of the parameters fit best. By moving the transposed Euler rotation matrix from equation 2-30 to the left hand side and taking $a^3/3F$ as a diagonal matrix c with the unknown constants c_1, c_2 and c_3 on its diagonal, the equation can be rewritten as,

$$Am = cAB_0. \tag{3-9}$$

Recall that in this set-up, the semi-major axis of the prolate spheroid is taken to lie in the x-direction whereas the two symmetric semi-minor axes lie in the y and z-direction. Hence, the form matrix F, and therefore the diagonal matrix c replacing it have the same value for the corresponding y and z-entries, c_2 and c_3 respectively, and are therefore equal.

Taken the Euler rotation matrix from equation 2-29, the unknowns c_2 and c_3 can be calculated with the aid of equations 3-10 and 3-11 respectively,

$$c_2 = \frac{m_1 \sin(\phi) + m_2 \cos(\phi)}{B_{0X} \sin(\phi) + B_{0Y} \cos(\phi)}, \tag{3-10}$$

$$c_3 = \frac{-m_1 \sin(\theta)\cos(\phi) + m_2 \sin(\theta)\sin(\phi) + m_3 \cos(\theta)}{-B_{0X} \sin(\theta)\cos(\phi) + B_{0Y} \sin(\theta)\sin(\phi) + B_{0Z} \cos(\theta)}. \tag{3-11}$$

Note that the only unknowns that are left on the right hand side are the azimuth and dip angle, all the rest of the parameters, the magnetic moment and Earth's inducing field, are known. Since c_2 and c_3 are equal, we can simply subtract the right hand side of equation 3-10 from 3-11 and take its absolute value to get the objective function for which we want to find the ideal combination of azimuth ϕ and dip angle θ,

$$\psi(\phi, \theta) = \min(|c_2(\phi, \theta) - c_3(\phi, \theta)|) \to 0. \tag{3-12}$$

An example of the $\phi - \theta$ grid to be searched for its minimum is shown in Figure 3-2. The orientation of the prolate spheroid used in this example is at $\phi = 135$ and $\theta = 25$ degrees. Without any guess on the value of ϕ or θ however, there is an infinite amount of possibilities as the yellow-coloured curve in Figure 3-2 contains many minima. It has not been examined

what kind of minima they are or if it is perhaps one large global minima, but either way it shows that either one of the two angles needs to be know to find the matching minimum and determine the other angle. To determine one or both of the angles, another piece of sensor should be used in combination with the magnetometer sensors.

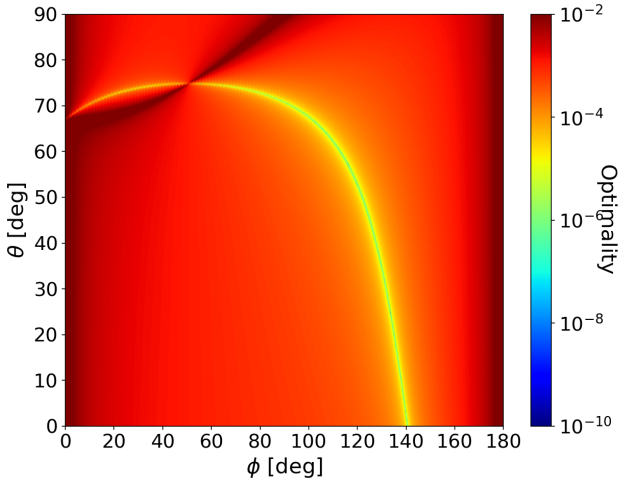

Figure 3-2: Grid search for an object with an azimuth of 135 degrees and dip of 25.

3-2-2 Inversion for UXO type and susceptibility

Given that the orientation of the object is determined correctly, the next step is to determine if the detected object can be fit in a prolate spheroid model. If it can be fit as being a prolate spheroid, the algorithm will list the object as an UXO. To answer this question, the radius, stretch factor and magnetic susceptibility of the object need to be estimated.

The susceptibility is not per definition specifically bound to a (type of) UXO, but it is necessary to determine its value as it will influence the stretch factor and radius and thus the fit of the model. I suggest using another two step system to first determine the radius and stretch factor and second the magnetic susceptibility.

Starting off with the determination of the stretch factor and radius. Recall that setting-up the initial estimates of the magnetic moment for the point source inversion in section 3-1-3 uses information from the desk-study. It is assumed that this information contains which types of UXO are expected to be found in this area and hence what kind of shape these UXO's have. This same information can be used to test which of the UXO types, with their corresponding length and radius, matches the anomaly. Finding the best fitting UXO - with respect to its stretch factor and radius - is just a matter of trail and error. An arbitrary but constant susceptibility value can be used in this stage.

Then second, after finding the best matching UXO type, the corresponding susceptibility needs to be determined. Making an initial guess on the susceptibility is not possible based on the data and can vary among UXO's, so a wide range of values needs to be examined. A

combination between a global search over the wide range of possibilities and local optimization is recommendable to retrieve a high accuracy when there is no good initial guess, so we can again use the Basin-Hopping inversion as described in section 3-1-2-1.

Again we will be using the GNRMS for the Basin-Hopping inversion, but d_{obs} and d_{est} from equation 3-8 are now the retrieved magnetic moment from the point source inversion and the reconstructed magnetic moment of a prolate spheroid with the aid of equation 2-30. If the GNRMS is below a certain treshold, which can vary depending on e.g. the data quality or clients preferences, the object will be classified as a UXO. If the GNRMS remains high and above the threshold, the object is classified as a non-UXO.

Chapter 4

Results

To answer the two research questions, two different datasets are used. This result section is dived into two parts accordingly, being:

1. A synthetic set of datasets for both TMI and vector data, processed with the algorithm described in chapter 3
2. A TMI dataset both processed with Oasis Montaj and with the agorithm from chapter 3

This two part division is made since there is no dataset available which contains both vector and TMI data, thus, for the comparison between the TMI and vector data, a synthetic dataset needed to be used. To also compare the TMI inversion to the industry standard Oasis montaj, the second part is added. This is important to make a reasonable comparison in chapter 5 and answer the research questions properly.

Both the real and synthetic datasets are located in the North Sea and have therefore a similar small declination, around 0 degrees, and large inclination, around 70 degrees. So although the two datasets will not be compared, it is expected that their behaviour is similar.

4-1 Part A North sea synthetic survey

The synthetic data example of part A are a subset of noise-free datasets where several parameters involved are varied. All datasets are constructed to be theoretically located in the same area, approximately 25km from the coast of the Hague, Netherlands at 52.196143 North, 3.893467 East. At this location, the declination of the Earth's magnetic field is 1.7592 degrees East and the inclination is 67.2497 degrees North with a field strength of 49315.9 nT dated on April 5th, 2022 [national oceanic atmospheric administration US department of Commerce, ND]. It should be mentioned that there is an uncertainty of 0.39 and 0.21 degrees for the declination and inclination respectively and of 145 nT for the field strength. For simplicity, the inclination, declination and field strength are assumed to be accurate and errors created by inaccuracies in the $\mathbf{B}_0$-field are disregarded.

Aside from sharing the same location, the datasets also share the same survey design, shown in figure 4-1. The survey consists of five parallel lines with a linespacing of 1m, comparable to a real-life survey. The in-line sampling distance is set to 0.04m, which is approximately 10x denser than an actual survey. The flight height is 5m above a flat surface and the UXO is located at (0,0,0).

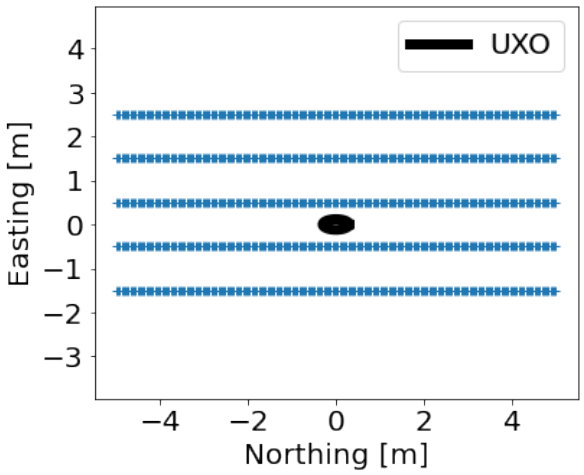

Figure 4-1: Survey design for the synthetic dataset, where the lines run from -5m to 5m North with a 0.04m inline spacing and are located at 0.5, 1.5 & 2.5m East of the object and 1.5 & 0.5 West of the object which is located at $(0, 0, 0)$.

Although the survey design for both the vector and total field magnetometers is the same, the vector magnetometers sample three times as much data as the total field magnetometers. Each 0.04m, the total field magnetometers only measure the total magnetic intensity whereas the vector field magnetometers measure the three components individually. I chose to keep the survey design the same rather than compensating for the TMI to show the benefits of only changing to vector magnetometers rather than rethinking and discussing the survey design.

Lastly, let's discuss the differences between each data set. The parameters that are varied are all included in the magnetic moment; the stretch factor, radius, orientation and magnetic

susceptibility. For the stretch factor and radius, a set of five UXO's are modelled as if they were true prolate spheroids, an overview of them can be found in table 4-1. The values used for the other three parameters, the azimuth, dip angle and susceptibility, are given in table 4-2. Using every single combination possible for the parameters from table 4-1 and 4-2, a total of 3.000 datasets were generated, which leads to 600 per UXO.

Table 4-1: A set of five airdropped ammunition retrieved from a Fugro archive.
** The shape used still is a prolate spheroid, it only specifies with tail as a reason why the stretch factor is longer, i.e. to compensate for the tail.*

Explosive	**Radius [m]**	**Stretch factor**	**Volume** $[m^3]$
Brisantbomb GP 250 lb without tail	0.1295	2.5	$2.2742 \cdot 10^{-2}$
Brisantbomb GP 250 lb with tail*	0.131	3.9	$3.6725 \cdot 10^{-2}$
Brisantbomb SC 250 lb	0.184	3.2	$8.3501 \cdot 10^{-2}$
Brisantbomb GP 500 lb	0.164	2.9	$5.3581 \cdot 10^{-2}$
Brisantbomb SC 500 lb	0.229	3.2	$1.6097 \cdot 10^{-1}$

Table 4-2: Parameters used to construct the field for all sub-datasets.

	Azimuth ϕ [deg]	**Dip angle** θ [deg]	**Magnetic susceptibility** χ
Values	[0, 20, 40, 60, 80, 100, 120, 140, 160, 180]	[0, 10, 20, 30, 40, 50, 60, 70, 80, 90]	[1, 10, 20, 50, 100, 200]

The main goal of this set-up is to first examine the robustness of the inversion against each parameter involved and second to get an insight in general how well both the vector data and TMI inversion perform. The TMI and vector data will be portrayed next to each other in the following sections.

4-1-1 Centre location

The initial estimate of the centre location to be plugged in into the point source inversion is determined as described in section 3-1-3-1. This means that the initial estimates of the centre location between the TMI inversion and the vector component inversion differs and is unique for each sub-dataset.

The point source inversion result for the centre location (x_0, y_0, z_0) are shown in Figure 4-2. The TMI shows a much wider range of values in Figure 4-2a which seem to be located further away compared to the rather precise vector field inversion result in Figure 4-2b. When it comes to the centre location, it can be observed that the vector data results are an order 10^{-8} more precise for y_0, 10^{-7} for x_0 and 10^{-7} for the estimated depth z_0.

The vector field results for the centre location moreover show a cross-like structure in the horizontal plane. As the x_0 deviates further away from the true location towards the positive side, y_0 deviates further away from the true location in the negative side, indicating a com-

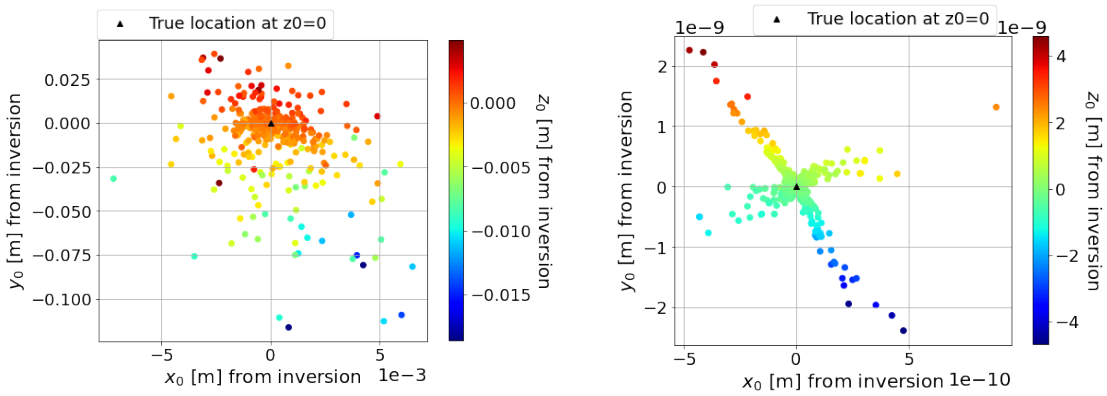

(a) TMI (x_0, y_0, z_0) inversion result

(b) Vector (x_0, y_0, z_0) inversion result

Figure 4-2: The resulting centre location after the Gauss-Newton (for the vector data) and Basin hopping (for the TMI data) inversion.

pensation mechanism in which even z_0 does its part and react to the movement in x_0 and y_0. This phenomena is not visible at all in the TMI results.

4-1-2 Magnetic moment

The first guess for the magnetic moment is, unlike for the centre location, the same for both the TMI and vector point source inversion. For each of the five UXO's from table 4-1, the maximum and minimum values of the UXO's are shown in table 4-3.

Table 4-3: The initial estimates of the magnetic moment for each explosive type.

Explosive	m_1 **initial** $[Am^2]$	m_2 **initial** $[Am^2]$	m_3 **initial** $[Am^2]$
Brisantbomb GP 250 lb without tail	63.5	-26.0	127.5
Brisantbomb GP 250 lb with tail	97.5	-53.0	210.5
Brisantbomb SC 250 lb	224.5	-110.0	470.5
Brisantbomb GP 500 lb	145.5	-67.0	300.0
Brisantbomb SC 500 lb	432.5	-212.5	906.5

Figure 4-3 shows the magnetic moment results from the GN or BH inversion of the point source versus the true magnetic moment of the synthetic dataset. Ideally, the plots should show a linear function with a slope of 1 and intersection at 0, or rather; the values on the x-axis and y-axis should be identical. The m_1, m_2 and m_3 from the vector data inversion indeed shows this exact linear trend in Figures 4-3b, 4-3d and 4-3f. The absolute differences between the true magnetic moment and the result from the inversion are at largest in the order 10^{-7}.

The TMI generally shows the same linear trend except for the m_2 results. Figure 4-3c shows that as as the true value of m_2 is close to zero Am^2 or smaller, some results deviate from the

ideal line. Especially when m_2 is zero, the largest absolute difference observed is 119.82 Am^2 . Whereas the largest absolute difference for m_1 is 8.24 Am^2 and for m_3 it is 17.14 Am^2.

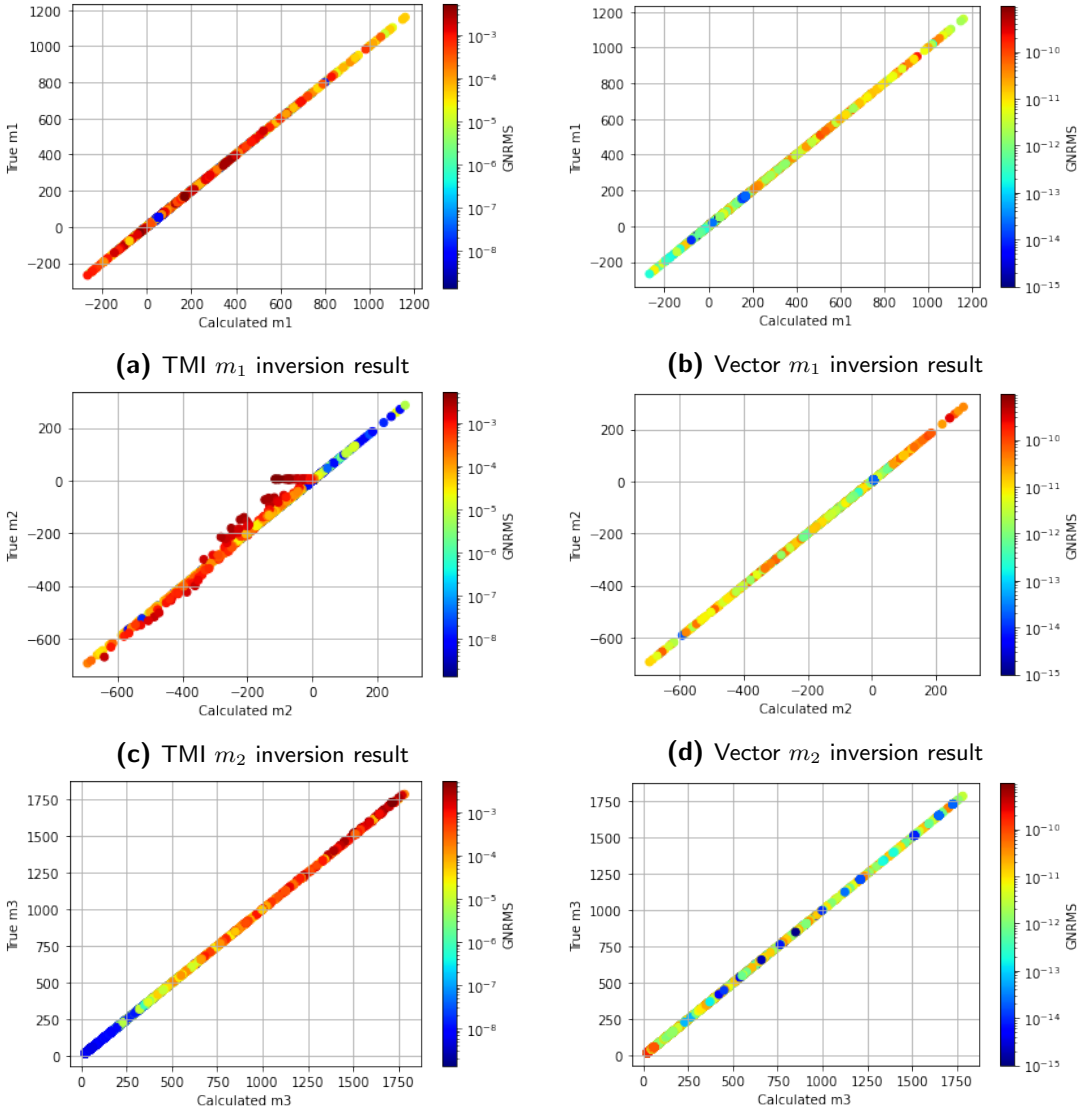

(a) TMI m_1 inversion result

(b) Vector m_1 inversion result

(c) TMI m_2 inversion result

(d) Vector m_2 inversion result

(e) TMI m_3 inversion result

(f) Vector m_3 inversion result

Figure 4-3: The resulting individual magnetic moment components after the Gauss-Newton (for the vector data) and Basin hopping (for the TMI data) inversion.

4-1-3 UXO type and susceptibility

Since the retrieval of the orientation is based on the accuracy of another type of sensor, this step is not part of the thesis and will be skipped over. To be able to do the UXO type inversion, it will be assumed that the orientation used in this prolate spheroid inversion is exact and does not contain errors. The exact values from Table 4-2 for the azimuth and dip angle are used.

This inversion will embroider on the results from the point source inversion, hence the magnetic moment retrieved in section 4-1-2 will be used as the observed data d_{obs}.

First, we need to determine which UXO fits the data best. Each one of the five UXO's from Table 4-1 is tested on every sub-dataset. All of them are given an arbitrary chosen but constant susceptibility of 30. After calculating the GNRMS errors between the retrieved magnetic moment from the point source inversion, and the calculated magnetic moment from the UXO's, d_{est}, the UXO type with the lowest GNRMS is picked to be the best fitting UXO type for each individual sub-dataset. The Basin-Hopping inversion to recover the true value of χ is only run on the best-fitting UXO type.

The TMI and vector inversion perform similarly if it comes to correctly classifying the UXO's: out of the 3000 sub-datasets, 2162 models are characterised correctly, corresponding to 72.07%. Figure 4-4 shows the correct and false classified groups with respect to the GNRMS from the point source inversion and the GNRMS from the final result the prolate spheroid inversion, including the optimization of the magnetic susceptibility. Note that the GNRMS of the prolate spheroid inversion is calculated based on the magnetic moment whereas the point source inversion uses the **B**-field to calculate the GNRMS.

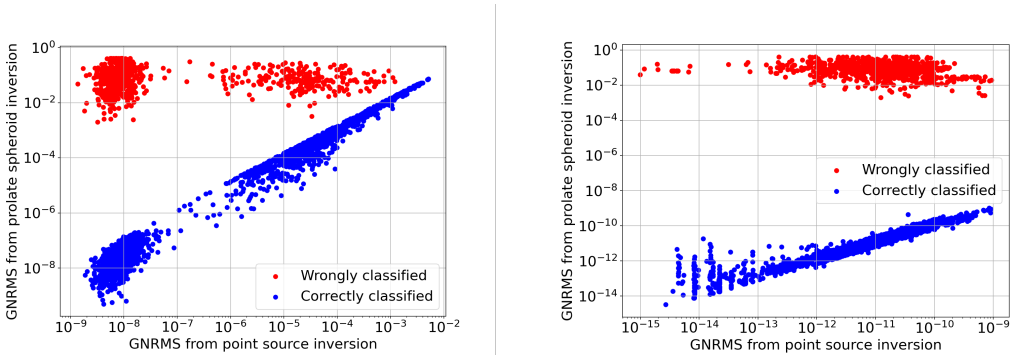

(a) TMI UXO classification **(b)** Vector UXO classification

Figure 4-4: Classification of the UXO based on the magnetic moment from 4-3 tested for five UXO's with $\chi = 30$. After finding the right UXO, χ is optimized to minimize the GNRMS the prolate spheroid inversion.

The correctly classified UXO's in Figure 4-4 imply that as the first inversion for the centre location and magnetic moment is more accurate, so will the second inversion for the shape and susceptibility of the UXO; the GNRMS of the point source inversion functions as a plateau for the error in this last step.

The susceptibility tries in vain to correct the wrongly classified parameters as can be seen in Figure 4-5. The vector data and TMI inversion again perform similarly, on both cases, most of the wrongly classified sub-datasets seem to contain a UXO with a low susceptibility.

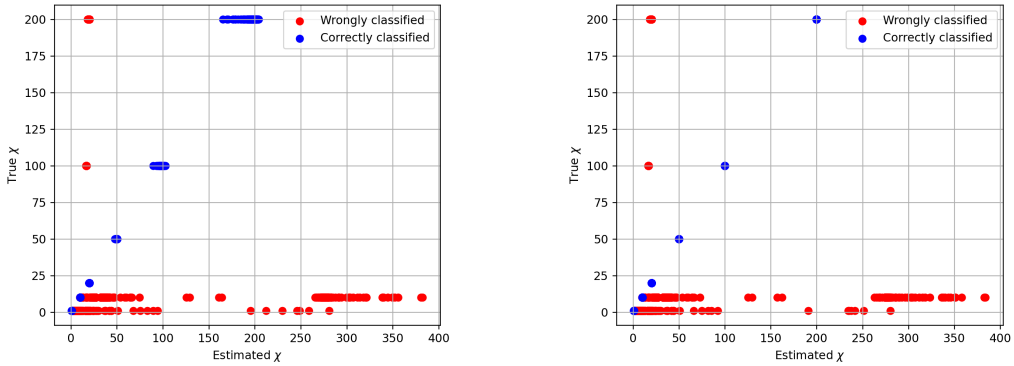

(a) TMI χ inversion result **(b)** Vector χ inversion result

Figure 4-5: The susceptibility from the inversion versus the true susceptibility.

4-2 Part B Real dataset

The dataset used in part B is chosen as it is an excellent starting point for the first real-life examination due to its simplicity and clean data as can be seen in Figure 4-6. The dataset however has also a downside; there is no imformation on the object(s) found in the area or which UXO's were expected to be found. Hence, for the inversion method, only the point source inversion will be conducted as there is too little information to conduct the prolate spheroid inversion.

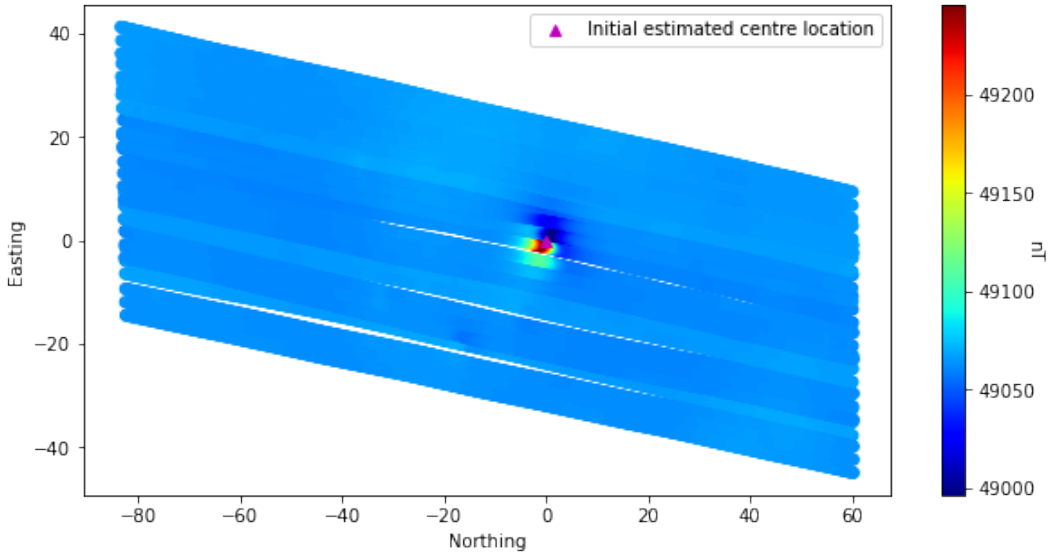

Figure 4-6: The dataset with raw TMI data on an imaginary grid with at (0,0) the initial estimated centre location.

The dataset contains only one large anomaly with an amplitude of 249.6 nT whereas the rest of the survey is rather homogeneous with some gradual fluctuations of maximum 20 nT. Figure 4-6 shows the dataset and the initial estimate of the centre location as derived with the

method from section 3-1-3. The coordinate system has been adapted such that this estimated centre location is located at (0,0) in the horizontal plane. Aside from correcting the GPS and filtering out peaks, created by malfunction during the survey, the data is unfiltered and contains the Earth's magnetic field as well as other types of noise.

The algorithm as discussed in chapter 3 is built for a residual field. Therefore, first the $\mathbf{B}_0$ field needs to be eliminated which is done with equation 2-37. The Earth's inducing field is taken to be constant over the extend of the small survey area and is calculated with the coordinates of the estimated centre location. Its strength is 49051.9 nT with a declination of -0.9349 degrees and inclination of 66.8394 degrees.

The same field has also been processed with the aid of Oasis Montaj to get a residual field. The OM method not only filters out the Earth's inducing field, but also takes care of other noise sources. Both the calculated residual field and the field from Oasis Montaj are shown in Figure 4-7.

It should be noted that the calculated residual field in Figure 4-7a only eliminates the Earths inducing field, but other noise sources are still present which is different to the procedure in OM. Therefore, Figure 4-7b looks much smoother further away from the anomaly than the calculated residual field. One other difference is that the amplitude of the anomaly in the Oasis Montaj field has increased to 252.5 whereas the calculated residual field has the same amplitude as the measured total field.

The Basin-hopping inversion will be run over the full extend of both residual fields. The initial estimate of the horizontal location was stated before to be (0,0), at a depth of 1.34m below the surface. Since no prior information is available on what kind of object we are dealing with, making an initial estimate of the magnetic moment is not possible. For the following results, the initial estimate for the magnetic moment has been set to be (1,1,1).

4-2-1 Inversion results

First, lets have a look at the inversion results, which are shown in table 4-4. The estimation of the centre location for both the inversion over the calculated residual and the residual from OM are very similar; x_0 differs with 0.058m, y_0 with 0.092 and z_0 with 0,044 from each other.

The variations in the magnetic moment on the other hand deviate much more, where there is a difference between the two results of 153.506, 632.540 and 45.623 for m_1, m_2 and m_3 respectively.

Table 4-4: Results after the Basin-hopping inversion for both the calculated residual field and the field filtered in Oasis Montaj

Model parameter	Calculated residual	OM residual
x_0	-0.460	-0.418
y_0	-0.351	-0.259
z_0	0.782	0.826
m_1	3139.799	3293.305
m_2	2792.559	3425.099
m_3	2919.164	2873.541

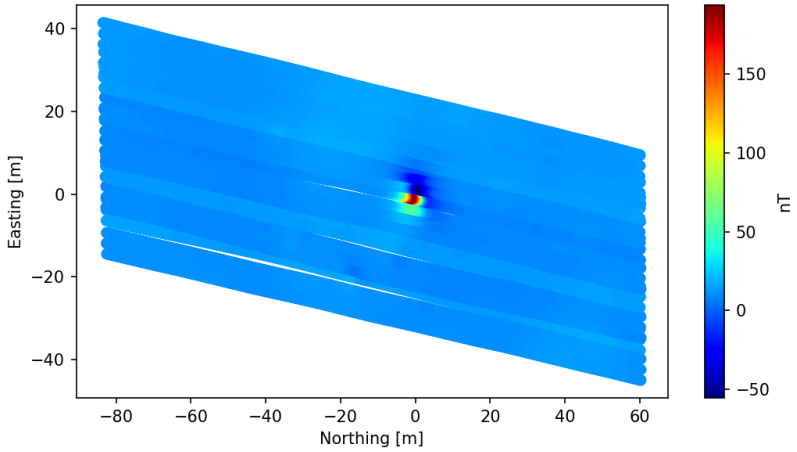

(a) Calculated residual

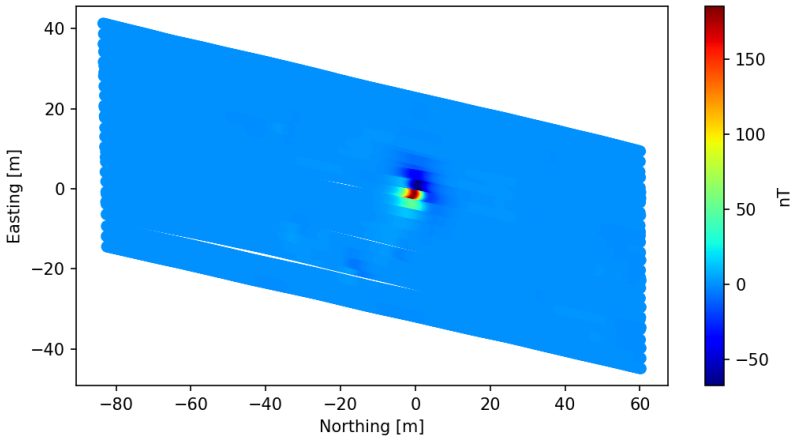

(b) Filtered residual in Oasis Montaj

Figure 4-7: The residual field used for the inversion where 4-7a is the calculated residual by subtracting the Earth's inducing field from the measured TMI field with the aid of equation 2-37 and 4-7b is the residual field created by filtering of the data in Oasis Montaj.

4-2-2 Oasis Montaj results

After running the newly developed inversion methodology, let's have a look back at the original industry standard results. Target picking is done on the Analytical Signal map created from the residual field shown in Figure 4-7b [Nabighian, 1972]. The resulting analytical signal is visualised in Figure 4-9 with a grid cell size of 0.5m and a blanking distance of 2m. It shows significantly more heterogeneity than could be observed in the TMI plot and could indicate that there is more than one magnetic object in the area which are missed in the visual inspection in the previous section. Only the anomalies which have a half amplitude of at least 6.0 nT are examined in this report, which is chosen such that only the one anomaly also processed in the inversion remains. The targets centre location is picked initially in the middle of the AS anomaly at 0.4107m North and 0.6795m East and at a depth of 0.4413m.

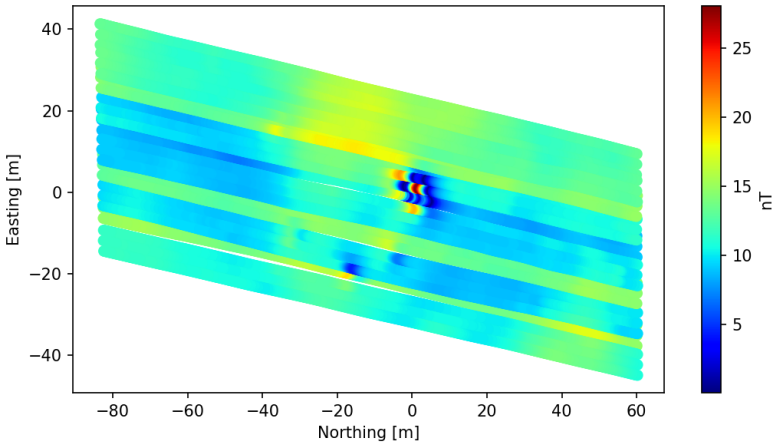

(a) Result from calculated residual

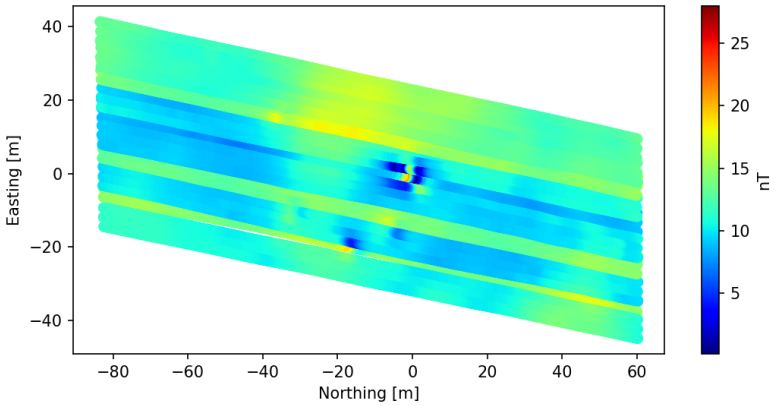

(b) Result from filtered residual in Oasis Montaj

Figure 4-8: The difference between the TMI field from Figure 4-6 and the reconstructed field with the parameters from table 4-4 for both methods.

Although generally not used, Oasis Montaj contains the tool to model the object and determine amongst others its weight, radius and magnetic moment. How Oasis Montaj sets-up this model is however hidden within the program. Rather than the magnetic moment vector, OM returns the norm of the magnetic moment, which is given to be 56.267 Am^2 for an object of 204.784076 kg with a median radius of 4.54m. Lastly, the modelling moreover updates the centre location towards a value of -0.414m North and -0.247m East at 0.695m below the surface.

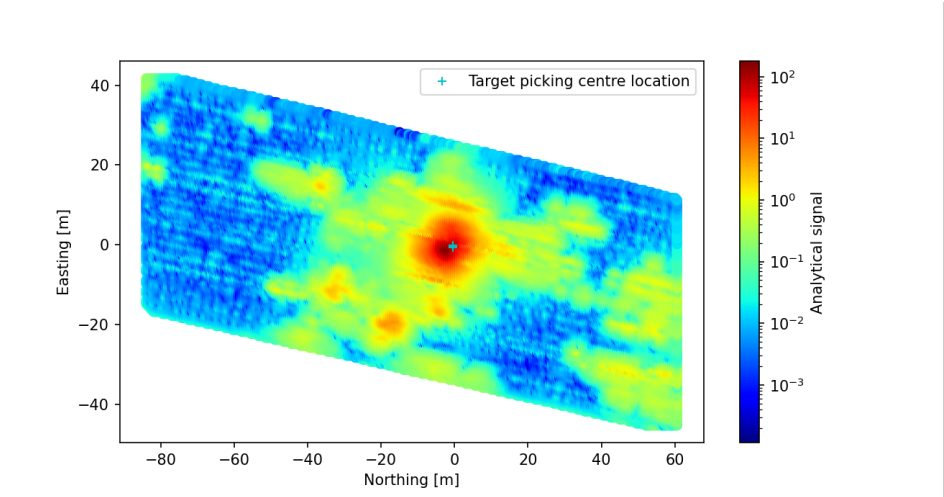

Figure 4-9: The analytical signal created in Oasis Montaj by using a grid cell size of 0.5m and a blanking distance of 2m with the target picked at $(0.4107, 0.6795, 0.4413)$.

Chapter 5

Discussion

After successfully running the TMI inversion on a synthetic and real dataset and the vector data inversion on a synthetic dataset, this chapter will zoom in on what can be learned from these results. The set-up of the discussion is the same as the results chapter 4; starting with the synthetic dataset of part A followed by the real dataset of part B.

5-1 TMI vs vector data inversion

Although the feasibility in a real life case is yet to be examined, the results for the synthetic data look promising. Both the TMI and vector data inversion algorithm still needs a lot more development before it can be used in real life, but we in this chapter limit ourselves to what can be observed from the results in chapter 4.

5-1-1 Point source ivnersion

Looking back at Figures 4-2 and 4-3, the vector data inversion seems to always deliver whereas the TMI inversion does not always perform well. This can also be concluded from the GNRMS. Figure 5-1 shows the GNRMS of the Basin hopping TMI inversion versus the GNRMS of the Gauss-Newton vector data inversion. The TMI shows more or less two clusters, one dense cluster located around 10^{-8} and a widespread cluster with higher values.

For these synthetic datasets, the best TMI inversion results, with the lowest GNRMS being $1.362635 \cdot 10^{-9}$, are an order worse than the worst vector data inversion results, where the highest one is $9.329265 \cdot 10^{-10}$. From this it could be concluded that the Basin-hoping inversion for the TMI does perform well in some cases, but always less than the Gauss-Newton inversion. Although the vector data yields more accurate results, in reality, the TMI results might already be accurate enough to the clients requirements.

Without placing a judgement on which GNRMS error is the minimum necessary to get a sufficient result, it is however worrying how wide the GNRMS errors resulting from the TMI

inversion range. The cluster around 10^{-8}, where all data poitns with a GNRMS smaller than 10^{-7} are categorised in, represents 61.3% of the 3000 datasets, whereas the remaining 38.7% take on values up to the order 10^{-2}.

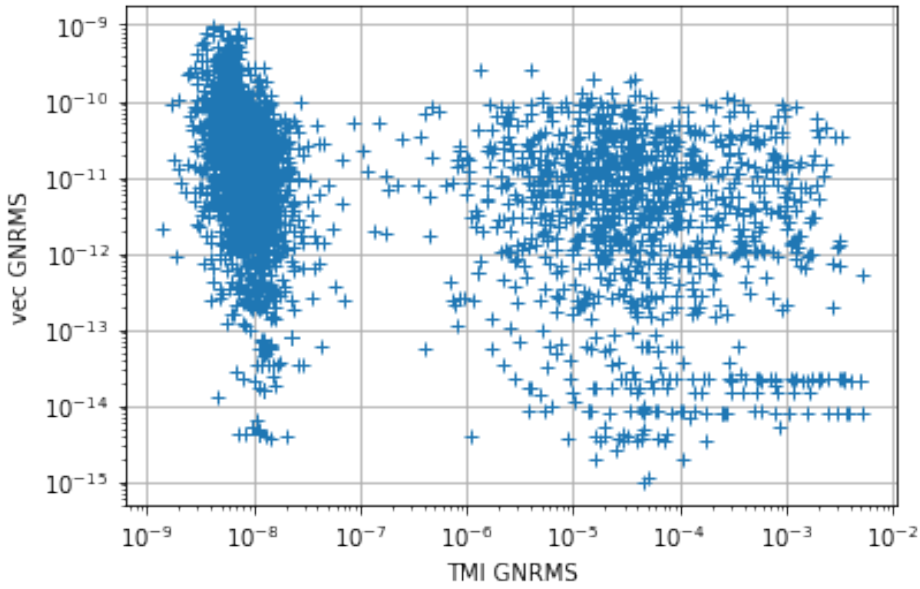

Figure 5-1: GNRMS of the 3000 models processed with only vector data vs TMI data

Having a closer look at a subset of the TMI results with a GNRMS in the order 10^{-3} or higher, it becomes clear that the Largest UXO, the Brisantbomb SC 500 lb in this case, is the main contributor with 94.6% of the in total 78 results. The remaining five cases with a GNRMS of 10^{-3} or higher are created by the second largest UXO, the Brisantbomb SC 250 lb. Another factor these results have in common is that they all have a dip angle of at least 50 degrees and the highest GNRMS is created in the datasets where the object has a dip angle of 90 degrees.

Given the fact that the largest UXO with a 90 degree dip angle creates the highest GNRMS could also already be argued, and thus confirmed, from the magnetic moment results of m_2 and m_3 in Figures 4-3c and 4-3e. The m_3 results of the TMI show that as m_3 increases, so does the GNRMS error. The parameter evaluation in section 2-4 indeed showed that as the radius and/or stretch factor increases, so does the amplitude of the **B**-field and its scaling magnetic field. The m_3 moreover increases when the object aligns with the z-component of the Earths magnetic field. On the other hand, the value of m_2 is very small at 90 degrees angle and Figure 4-3c indeed shows the largest deviations around zero.

On the contrary, the highest GNRMS values in the vector data inversions are created by the two smallest UXO's, the brisantbomb GP 250. On the contrary with the TMI results, the dip angle seems to be irrelevant in the matter. Although less obvious, this could again be argued by looking at the m_3 result in Figure 4-3f where the highest GNRMS corresponds to the lowest m_3 values.

5-1-2 Prolate spheroid inversion

The inversion to retrieve the azimuth and dip angle of the object has not been put in practice in the scope of the thesis as it depends on data from another sensor. Before adapting the methodology, an error sensitivity analysis should be made. Including how accurate the sensor measuring the orientation needs to be for a sufficient result within a yet to be defined threshold as well as how bad the next inversion becomes when this step includes errors.

Moving on to the UXO-type determination and its magnetic susceptibility shows that this step is rather robust where 72.07% of the synthetic sub-datasets is correctly classified. Following the outcome of the synthetic dataset results, miss-classification seems to mainly occur in two particular cases: 1) a UXO with low magnetic susceptibility and 2) the GP 250 lb with tail. Out of the in total 838 miss-classified cases, 747 (89.14%) have a susceptibility lower than the estimated susceptibility of 30. The second case is responsible for 282 cases, or simply 33.65 %. Note that case 1 does not exclude case 2 and vice versa.

First, let's discuss the second case. Why is the GP 250 lb Brisantbomb with tail performing so much worse than the others? Looking back at its shape, Table 4-1 shows that it stands out from the others when it comes to its large stretch factor of 3.9. From the form matrix (equation 2-25) it can be observed that the stretch factor and magnetic susceptibility are both part of the denominator and hence chances are that larger stretch factors need a more accurate susceptibility before it can be recognised accurately due to a codependency between the two.

Second, table 5-1 gives the misclassification per UXO with respect to the magnetic susceptibility. The Brisantbomb 250 lb with tail is the only one that gets misclassified with high magnetic susceptibilities. For the SC 250, GP 500 and SC 500, it can be observed that roughly 1/3 of its sub-datasets are miss-classified, which corresponds perfectly to the two out of the six lowest χ values, 1 & 10, used in the synthetic subsets. This indicates that the system fails for most low magnetic susceptible objects.

Table 5-1: Percentage of missclassification per each of the five UXO's. Each UXO occurs in 600 sub-datasets where the magnetic susceptibility and orientation differ.

UXO type	**% missclassifed**	χ
Brisantbomb GP 250 lb without tail	1.17%	1, 10
Brisantbomb GP 250 lb with tail	47 %	1, 10, 100, 200
Brisantbomb SC 250 lb	32.17 %	1, 10
Brisantbomb GP 500 lb	29.5 %	1, 10
Brisantbomb SC 500 lb	29.8 %	1, 10

5-1-2-1 Sensitivity analysis

Estimating the correct susceptibility from the start is thus rather important to determine which UXO fits the estimated magnetic moment best. More importantly in the end however is determining if any UXO-model describes the object well or if we are likely dealing with a non-UXO. The role of the magnetic susceptibility becomes even larger in this latter case.

The synthetic datasat only contained a total of five UXO's with each a unique combination in χ and its orientation. As an example, the synthetic sub-datasets are filtered to only contain the datasets which contain a UXO with a susceptibility of $\chi = 20$. Moreover, the UXO's are here all classified correctly, discarding the prolate spheroid inversion results form section 4-1. The remaining 500 sub-datasets are examined on how sensitive the GNRMS of this prolate spheroid inversion is with respect to a correct result of the magnetic susceptibility. Using the magnetic moment as derived from the point source inversion and taking all other parameters to be exactly true leads to the plots in Figure 5-2. A total of six different susceptibilities are plugged into the magnetic moment equation of a prolate spheroid (equation 2-30), with values,

$$\chi_{est} = \chi_{true} - 10^h,$$

where $h = 0, -1, -2, -3, -4, -5$. Figure 5-2a shows that for each 10^1 accuracy increase, the GNRMS also decreases by 10^1. In reality, this relationship will vary depending on the susceptibility; at an accuracy of 10^{-4} for $\chi = 20$, the GNRMS is around 10^{-6}, in the same case for a susceptibility of 200, the same GNRMS values of around 10^{-6} are reached at an accuracy of only 10^{-2}, which is two orders smaller. This is one of the reasons why a global brute grid search would not suffice as it will likely not get high enough accuracy in most cases without running an excessive and dense grid.

From Figure 5-2b, a whole other lesson can be learned, namely the importance of a good performing point source inversion. As soon as the GNRMS of the inversion for the centre location and magnetic moment becomes higher than 10^{-6}, it becomes impossible to fit the model with a GNRMS below 10^{-6}. Hence, it will get more difficult to distinguish between UXO's and other material. It can be concluded that the GNRMS of the prolate spheroid inversion will always remain lower than the GNRMS of the point source inversion.

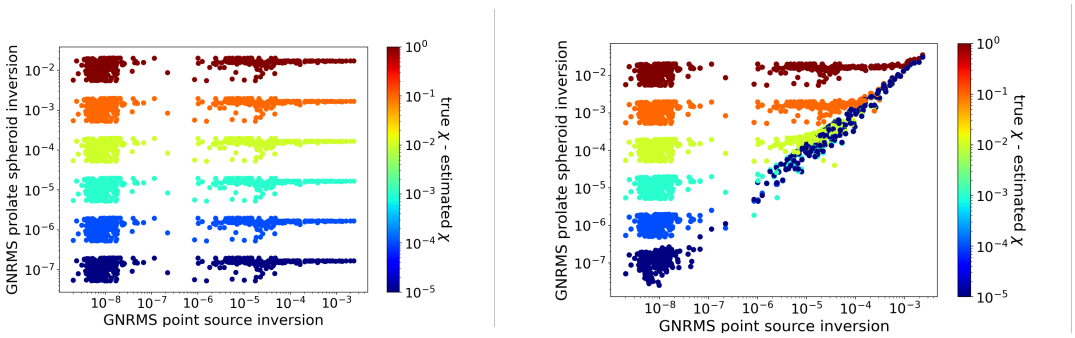

(a) Vector **(b)** TMI

Figure 5-2: Magnetic susceptibility with accuracy's in the power tens for an object with $\chi = 20$ and an arbitrary shape and orientation according to Tables 4-1 and 4-2 respectively.

5-2 Algorithm vs Oasis Montaj

The GNRMS of the point source inversion of the calculated residual field is 0.916417 with 13482 function evaluations versus 0.151706 with 8307 function evaluations for the residual field

from Oasis Montaj. From these values one could argue that the the first inversion did not deliver, however it needs to be noted that the GNRMS is calculated with the aid of a residual field which still contains noise. The GNRMS of the inversion ran on the calculated residual drops to a value of 0.304462 when we take the OM residual field as d_{obs} instead. Although still high for GNRMS-norms, it shows that filtering can strongly reduce the GNRMS and therefore make it easier and faster to determine if the model does or does not fit well. However, even with noise, the system seems to be robust and the resulting values for the centre location is within close range, but the magnetic moment deviates a lot more.

The centre location found with the inversion algorithm agrees well to the one determined with the modeling tool of Oasis Montaj. Table 5-2 shows the relative difference of the OM results compared to the two inversion results from Table 4-4.

Table 5-2: The relative difference between the location estimation of the industry standard Oasis Montaj versus the inversion algorithm.

Centre location with respect to OM result	**inversion on calculated residual field**	**inverison on OM residual field**
Northing [m]	0.046	0.004
Easting [m]	0.104	0.012
Depth [m]	0.087	0.131
Total distance [m]	0.143	0.132

As much as the two methods agree on the centre location, the magnetic moment is the complete opposite. The inversion algorithm returns high values in the order 10^3 whereas Oasis Montaj finds a value not even in the order 10^2. Due to missing information on the (expected to be) found UXO, it is impossible to make a judgement which outcome represents reality better, but this large difference cannot go unnoticed and should be examined in more detail in the future.

Due to no available information on the object's properties, the prolate spheroid inversion cannot be run and this part is missing. Oasis Montaj on the other side is able to estimate some of the properties, amongst which the weight and median radius. The validity of these properties is however again not validated and question remains how they are determined.

Until proven otherwise, it looks like the inversion algorithm has the potential to unlock more information than the industry standard does currently. Instead of a median radius of the object, the prolate spheroid inversion supposedly can give two radii and the susceptibility. On the other hand, the industry standard has the ability with no prior information to retrieve some object parameters.

Chapter 6

Conclusion

This report describes a set-up for step-wise inversion algorithms for both vector and total field data inversion for magnetic UXO surveys. The goal of these new processing methodologies is to examine if vector data results in more favourable results and if UXO's can be distinguished from non-UXO's with the aid of a prolate spheroid model. The algorithm of the TMI inversion has moreover been compared to the current industry standard to examine if the new developments should be pursued. Section 6-1 and 6-1-3 will answer both partial-questions individually in more detail. The conclusions however serve only as an advice according to the results from this report; more research needs to be done. Section 6-3 will give some suggestions on how the research can potentially be moved forward towards a final decision.

6-1 Does vector data yield better results than TMI data on synthetic data?

The first and foremost topic of this thesis is to compare vector and TMI data. Due to the lack of actual vector data, question is stricly limited to synthetic datasets. The concluding arguments are approached from three sides namely, 1) the performance of both inversions, 2) the feasibility for a business case and 3) how important a good working point source inversion is for the prolate spheroid inversion. For this question, only the point source inversion is of importance as the prolate spheroid inversion is the same for both TMI and vector data. The only thing to keep in mind is that the prolate spheroid inversion depends on the results of the point source inversion and errors or inaccuracies made in this stage will be transferred on to next.

6-1-1 Performance

The accuracy of the Gauss-Newton inversion for the vector data is at least an order higher than the Basin-Hopping inversion for the TMI when we look to the Global Root Mean Squared

error. In some cases this difference is even higher where the GNRMS error rises to a problematic high power of 10^{-2}. Even though a decision has not been made on which values of the GNRMS are acceptable and which are not, it is clear that the GN vector inversion always delivers whereas the BH TMI inversion struggles with sub-datasets with long-streched UXO's with a large dip angle.

But the GNRMS is after all just an arbitrary error measurement. With the exception of the magnetic moment in the y-direction, m_2, the model parameters of the TMI inversion are reasonably accurate derived. Surely the estimation of the centre location of the vector data is only 10^{-9} m off utmost versus 10^{-1} m for the TMI data, but both are well within reason for the current 0.5 m threshold. Moreover, a GPS system offshore does not even have such a high accuracy, so those centimetres do not matter.

That being said, when moving forward to the prolate spheroid inversion, the accuracy of the magnetic moment derived from the point source inversion is very important. The GNRMS of the point source inversion forms for both TMI and vector data a plateau for the GNRMS error of the prolate spheroid inversion. It is not possible to get a well fitting model for any of the UXO's if the magnetic moment in the first inversion deviates too much. How much it can deviate to still get the correct outcome is not examined in this thesis, but the fact that it serves as a bottle neck for the prolate spheroid inversion, which is robust when used on its own, is undeniable.

6-1-2 Feasibility

The performance of the inversion on a small synthetic-noise free dataset can be perfect, but for it to be feasible for real-life cases is another story.

Recall that the vector data inversion uses a local optimization method, the Gauss-Newton inversion, whereas the TMI combines a global and local optimization in the more complex Basin-Hopping inversion. The Basin-Hopping inversion with over a thousand iterations is more computational expensive than the Gauss-Newton with only tens of iterations. This is not a problem for the synthetic dataset as it only contains one anomaly and a few datapoints, but this might have consequences for large datasets with a lot of anomalies which all need to be examined in the current set-up.

Another minor inconvenience that the TMI experiences is that for the BH-inversion to work properly, bounds need to be set. The boundaries used in this report worked perfectly for the synthetic data, but it remains a question how these will perform in a real-life situation.

To answer the question purely based on the results on the synthetic data, the Gauss-Newton vector data inversion yields better results. It shows robustness as it performs well on all of the tested scenarios. Moreover, the algorithm is fast and therefore well suited for the project-based surveys.

6-1-3 Relevance for the prolate spheroid inversion

Going a step further outside of the research question, the performance of the prolate spheroid inversion is bottle necked by the performance of the point source inversion, so it is of key importance to pick the best performing inversion technique based on the conclusion in 6-1.

Neglecting the retrieval of the azimuth and dip angle for now, the prolate spheroid inversion turns out to work well for a first attempt with 72.07 % of the UXO's classified correctly for the synthetic dataset.

On the other hand, the parameters within this prolate spheroid inversion need to be very accurate if we want to determine if the prolate spheroid model fits well. At as susceptibility of 20, if an accuracy of 10^{-6} is required, we can only deviate from 20 by a factor of 10^{-4}. Moreover, the exact values for the stretch factor and reality are used. In reality, the radius and stretch factor among UXO's can vary and there might be an uncertainty in its length and radius. It remains to be tested if the shape of a UXO is sufficiently similar to that of a prolate spheroid. This question remains open to be answered.

Differentiating between Unexploded Ordnances and other material can potentially be done with the prolate spheroid model, as long as magnetic moment, orientation and shape can accurately be derived or assumed

6-2 Does the two-step inversion have the potential to improve the current processing technique?

An attempt was done with the aid of the dataset in part B to lie the two methods next to each other for comparison. Both the industry standard Oasis Montaj and the basin-hopping inversion return centre location estimates within 0.15 m from each other. This indicates that if the BH inversion would only be used for the determination of the centre location, it would not be justifiable to change the current system.

As much as the two methods are in agreement on the centre location, the opposite is true for the magnetic moment. With a difference in the order 10^2, one of them must be very far off. Which one of the two that is cannot be determined as there is no information on what type of object created the anomaly.

This moreover makes it impossible for the TMI inversion algorithm as it is currently set-up to retrieve anymore information from the object. Oasis Montaj however has some more tricks up its sleeve and is able to determine object characteristics, but it is not possible to say how accurate these results are.

In short, I found the results inconclusive. Both methods have capabilities that the other one does not possess. The analytical signal in Oasis Montaj makes it a lot easier to spot anomalies, which would serve as a usefull tool for the inversion too. But the magnetic modelling tool in Oasis Montaj only returns the norm of the magnetic moment rather than its three (m_1, m_2, m_3) components.

To conclude, I would suggest that more research should be done to keep all options open. I expect that both methods have their upsides and that by partly combining them, the best result can be retrieved.

6-3 Outlook

The combination of a Gauss-Newton inversion on vector data to retrieve the magnetic moment and centre location of the object followed by a prolate spheroid inversion to retrieve the shape and magnetic susceptibility of the object looks promising, and I strongly reccomand looking further into this methedology. There still is a long road ahead to proof it is actual feasible and an even longer one to make it into a final product.

In this thesis, the work on comparing vector data and total field data was only conducted theoretically on a synthetic perfect dataset. In reality however, magnetometer UXO surveys are bothered by noise levels such as diurnal variations [Yamazaki and Maute, 2017]. It will be necessary to conduct a dummy survey with both TMI and vector sensors. In the early stages, it will be necessary to know all model parameters involved to check the validity. Aside from running these survey's on UXO's, it is also usefull to run survey's over non UXO's to examine the prolate spheroid inversion.

Bringing this technique to the real-world furthermore means that there will likely be multiple anomalies in each dataset. The algorithm should be updated such that it can locate multiple anomalies and run the inversion on a restricted area around the UXO which is not too much influenced by the other anomalies.

In addition to the processing part which was the topic of this thesis, other components of the UXO mitigation process should also be scrutinized. Filtering of noise was already shortly mentioned, but finding the optimal survey design can also lead to improvements.

Lastly, I firmly believe that having a UXO-database, possibly in combination with a non-UXO database, can help with the final classification as it gives an insight on what we are looking for. The database still needs to get a defined lay-out, but one can start with adding model parameters found from the inversions, its true parameters and how these relate to the measured field.

There is still a lot to be done in this exciting "new" field, but I am excited to continue this work at Fugro for the coming year.

Bibliography

[Altshuler, 1996] Altshuler, T. W. (1996). Shape and orientation effects on magnetic signature prediction for unexploded ordnance. *Proc. UXO Forum*, pages 282–291.

[Barbu and Zhu, 2020] Barbu, A. and Zhu, S. (2020). *Monte Carlo Methods*. Springer Nature Singapore Pte Ltd.

[Billings, 2004] Billings, S. (2004). Discrimination and classification of buried unexploded ordnance using magnetometry. *IEEE Transactions on Geosciences and Remote Sensing*, 42(6):1241 – 1251.

[Billings et al., 2002] Billings, S. D., Pasion, L. R., and Oldenburg, D. W. (2002). Discrimination and identification of uxo by geophysical inversion of total-field magnetic data.

[Blakely, 1995] Blakely, R. (1995). *Potential theory in gravity and magnetic applications*. Cambridge University Press.

[britisch geological survey, 2019] britisch geological survey (October 2019). International geomagnetic reference field (igrf). http://www.geomag.bgs.ac.uk/research/modelling/IGRF.html. Accessed: April 5th, 2022.

[Buttler, 2005] Buttler, D. K. (2005). *Nearsurface Geophysics*. Society of Exploration Geophysicists.

[Constales et al., 2017] Constales, D., Yablonsky, G. S., D'hooge, D. R., Thybaut, J. W., and Marin, G. B. (2017). *Advanced Data Analysis and Modelling in Chemical Engineering*. Elsevier.

[Cooper, 2004] Cooper, G. R. J. (2004). Euler deconvolution applied to potential field gradients. *Exploration Geophysics*, 35(3):165–170.

[Courtillot et al., 1992] Courtillot, V., Valet, J., Hulot, G., and Mouel, J. L. (1992). The earth's magnetic field: Which geometry? *EOS, Transactions, American Geophysical Union*, 73(32).

[Iwamatsu and Okabe, 2004] Iwamatsu, M. and Okabe, Y. (2004). Basin hopping with occasional jumping. *Chemical Physics letters*, 399:396 – 400.

[Krawczyk et al., 2018] Krawczyk, S., Sass, S., and Kluge, M. (2018). Historical investigation and risk mitigation for the identification of unexploded ordnance (uxo) in the north sea and baltic sea. *2018 IEEE/OES Baltic International Symposium (BALTIC)*.

[Maxwell, 1865] Maxwell, J. C. (1865). A dynamical theory of the electromagnetic field. *Philosophical Transactions of the Royal Society of London*, 155:459–512.

[McPhee, 1989] McPhee, J. (1989). Electromagnetic remote sensing: Low frequency electromagnetics. *Suffield special publication*, (124).

[Nabighian, 1972] Nabighian, M. (1972). The analytic signal of two-dimensional magnetic bodies with polygonal cross-section: Its properties and use for automated anomaly interpretation. *Geophysics*, 37(3):507–517.

[national oceanic atmospheric administration US department of Commerce, ND] national oceanic atmospheric administration US department of Commerce (N.D.). Magnetic field calculators. https://www.ngdc.noaa.gov/geomag/calculators/magcalc.shtml#igrfwmm. Accessed: April 5th, 2022.

[Nelson et al., 1998] Nelson, H. H., Altshuler, T. W., Rosen, E. M., McDonald, J. R., Barrow, B., and Khadr, N. (1998). Magnetic modeling of uxo and uxo-like targets and comparison with signature measured by mtads.

[Olson et al., 2012] Olson, B., Hashmi, I., Molloy, K., and Shehu, A. (2012). Basin hopping as a general and versatile optimization framework for the characterization of biological macromolecules. *Advances in Artificial Intelligence*.

[OSPAR, 2009] OSPAR (2009). Assessment of the impact of dumped conventional and chemical munitions (update 2009). https://www.ospar.org/documents?v=7110.

[Pederson and Stalcup, 1997] Pederson, A. and Stalcup, B. (1997). Phase iii advanced technology demonstrations at jefferson proving ground. *Proceedings of the UXO Forum*, 97:281–289.

[Stratton, 1941] Stratton, J. (1941). *Electromagnetic Theory*. McGraw-Hill Book Company, Inc.

[Thomson, 1982] Thomson, D. (1982). Euldpth: A new technique for making computer-assisted depth estimates from magnetic data. *Geophysics*, 47:31–37.

[Touzani and Rappaz, 2013] Touzani, R. and Rappaz, J. (2013). *Mathematical models for eddy currents and magnetostatics: with selected applications*. Springer, Dordrecht.

[Wales and Doye, 1997] Wales, D. J. and Doye, J. P. K. (1997). Global optimization by basin-hopping and the lowest energy structures of lennard-jones clusters containing up to 110 atoms. *Phys. Chem.*, 101(28):5111–5116.

[Wang et al., 2020] Wang, J., Shena, Y., Zhaod, R., Zhoud, C., and Gaoa, J. (2020). Estimation of dipole magnetic moment orientation based on magnetic signature waveform analysis by a magnetic sensor. *Journal of Magnetism and Magnetic Materials*, 505.

[Wang, 2012] Wang, Y. (2012). Gauss–newton method. *WIREs Comput Stat*, 4:415–420.

[Xiao and Lu, 2002] Xiao, Y. and Lu, Y. (2002). The prolate and oblate spheroid perfectly matched layers. *IEEE Transactions on Magnetics*, 38(2):669 – 672.

[Yamazaki and Maute, 2017] Yamazaki, Y. and Maute, A. (2017). Sq and eej—a review on the daily variation of the geomagnetic field caused by ionospheric dynamo currents. *Space Sciences Reviews*, 206:299–405.

Appendix A

Parameter evaluation

Figure A-1 shows how scaling the object with the aid of radius a results into different results.

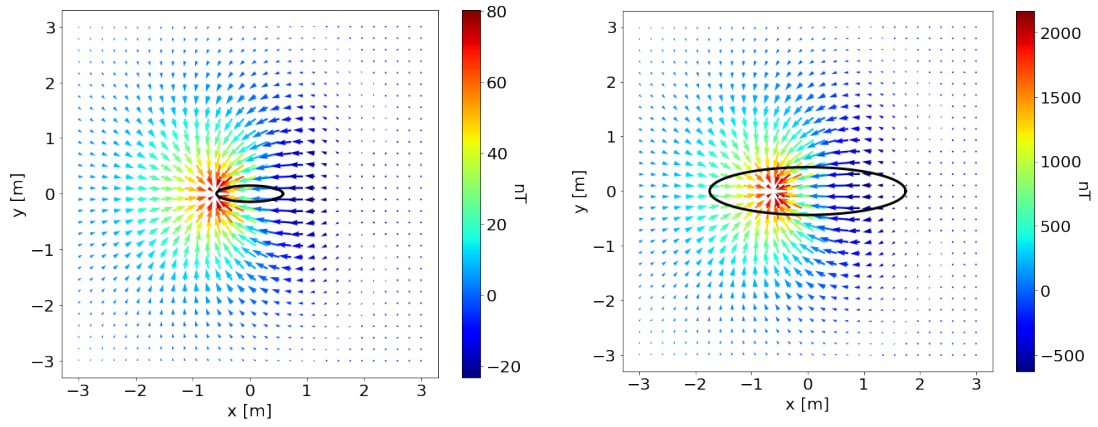

(a) $a = 0.15m$ **(b)** $a = 0.45m$

Figure A-1: Setting other radius values while keeping the rest the same as in Figure 2-3 shows a significant difference in field pattern.

Similarly to the radius, the susceptibility χ also seems to serve only as a scaler as is shown in Figure A-2.

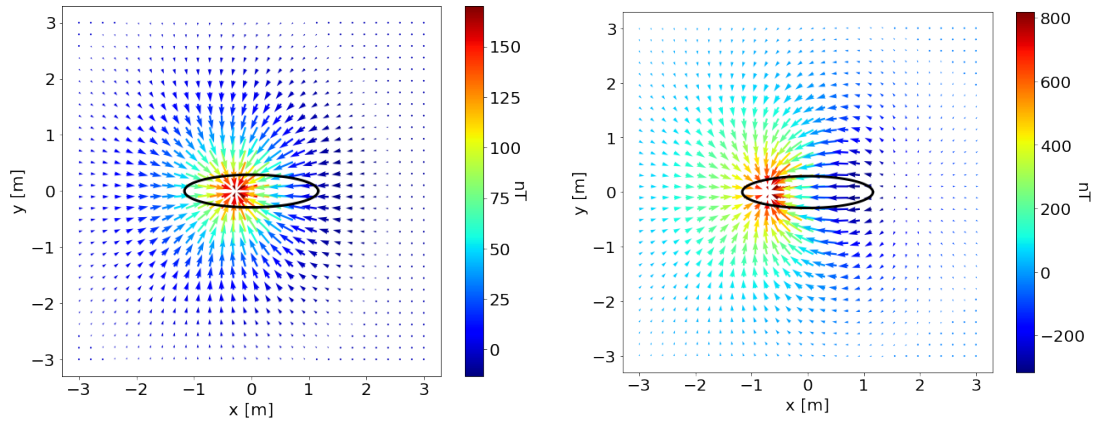

(a) $\chi = 1$ **(b)** $\chi = 100$

Figure A-2: Setting other magnetic susceptibiliy values while keeping the rest the same as in Figure 2-3 shows a significant difference in field pattern.

Appendix B

Derivative derivation jacobian step 1 inverison

The derivatives within the jacobian matrix for the vector components are derived analytically. As we are dealing with six unknowns, namely $(m_1, m_2, m_3; x_0, y_0, z_0)$, the jacobian consists of six columns and as many rows as there are data points. The shape of the jacobian is visualised in

$$J_{i,k} = \begin{bmatrix} \frac{\partial B_{i,k}}{\partial m_1} & \frac{\partial B_{i,k}}{\partial m_2} & \frac{\partial B_{i,k}}{\partial m_3} & \frac{\partial B_{i,k}}{\partial x_0} & \frac{\partial B_{i,k}}{\partial y_0} & \frac{\partial B_{i,k}}{\partial z_0} \end{bmatrix} \quad for \quad i = x, y, z \quad k = 1, 2, 3... \tag{B-1}$$

The following sections B-1, B-2 and B-3 will give an overview of the analytically derived derivatives.

B-1 Derivatives of B_x

The analytical solution for the B_x field can be written as,

$$B_x = \frac{1}{R^3}[3(m \cdot \hat{r})r_x - m_1], \tag{B-2}$$

where R is the distance between the object and sensor, r is the unit distance vector of R, m is the magnetic moment and r_x and m_1 are the unit distance vector and magnetic moment in the x-direction. To make it easier to differentiate, I decided to write out the inner product of $m \cdot \hat{r}$. For simplicity, I will write the distance between observer and sensor, i.e. $(x - x_0, y - y_0, z - z_0)$ as (X, Y, Z). This results into equation B-3,

$$B_x = \frac{3 \cdot (X^2 m_1 + XY m_2 + XZ m_3)}{R^5} - \frac{m_1}{R^3}. \tag{B-3}$$

Starting of simple with the derivation of the magnetic moment of the object, m_1, m_2 and m_3, one can observe that only the distances between sensor and object play a role,

$$\frac{\partial B_x}{\partial m_1} = \frac{3 \cdot X^2}{R^5} - \frac{1}{R^3}, \tag{B-4}$$

$$\frac{\partial B_x}{\partial m_2} = \frac{3 \cdot XY}{R^5}, \tag{B-5}$$

$$\frac{\partial B_x}{\partial m_3} = \frac{3 \cdot XZ}{R^5}. \tag{B-6}$$

The derivatives with respect to the centre location of the object (x_0, y_0, z_0) is a bit more complex as these both occur in the numerator and the denominator within R. Therefore we need to use a chain rule in the R^{-3} part and product rule and chain rule in the R^{-5} part. The derivatives of x_0, y_0 and z_0 are then as follows,

$$\frac{\partial B_x}{\partial x_0} = \frac{15X^2 \cdot (Xm_1 + Ym_2 + Zm_3)}{R^7} - \frac{3 \cdot (3Xm_1 + Ym_2 + Zm_3))}{R^5}, \tag{B-7}$$

$$\frac{\partial B_x}{\partial y_0} = \frac{15Y \cdot (X^2m_1 + XYm_2 + XZm_3)}{R^7} - \frac{3 \cdot (Ym_1 + Xm_2)}{R^5}, \tag{B-8}$$

$$\frac{\partial B_x}{\partial z_0} = \frac{15Z \cdot (X^2m_1 + XYm_2 + XZm_3)}{R^7} - \frac{3 \cdot (Zm_1 + Xm_3)}{R^5}. \tag{B-9}$$

As one would expect, the centre location and the magnetic mom in the x-plane have the highest contribution in the jacobian of B_x.

B-2 Derivatives of B_y

The derivatives of B_y show a very similar pattern, but now the y_0 and m_2, i.e. the centre location and magnetic moment of the object in the y-plane, are the biggest contributors. Let's rewrite B_y in a similar fashion as B_x in equation B-3, this results in,

$$B_y = \frac{3 \cdot (XYm_1 + Y^2m_2 + YZm_3)}{R^5} - \frac{m_2}{R^3}. \tag{B-10}$$

Then the derivatives with respect to m_1, m_2, m_3 are simply defined as,

$$\frac{\partial B_y}{\partial m_1} = \frac{3 \cdot XY}{R^5}, \tag{B-11}$$

$$\frac{\partial B_y}{\partial m_2} = \frac{3 \cdot Y^2}{R^5} - \frac{1}{R^3}, \tag{B-12}$$

$$\frac{\partial B_y}{\partial m_3} = \frac{3 \cdot YZ}{R^5}. \tag{B-13}$$

The derivatives of the centre location of the object are also derived in a similar, matter as for B_x as,

$$\frac{\partial B_y}{\partial x_0} = \frac{15X \cdot (XYm_1 + Y^2m_2 + YZm_3)}{R^7} - \frac{3 \cdot (Xm_2 + Ym_1)}{R^5}, \tag{B-14}$$

$$\frac{\partial B_y}{\partial y_0} = \frac{15Y^2 \cdot (Xm_1 + Ym_2 + Zm_3)}{R^7} - \frac{3 \cdot (Xm_1 + 3Ym_2 + Zm_3))}{R^5}, \tag{B-15}$$

$$\frac{\partial B_y}{\partial z_0} = \frac{15Z \cdot (XYm_1 + Y^2m_2 + YZm_3)}{R^7} - \frac{3 \cdot (Zm_2 + Ym_3)}{R^5}. \tag{B-16}$$

B-3 Derivatives of B_z

Same routine as for B_x and B_y, where we write B_z as,

$$B_z = \frac{3 \cdot (XZm_1 + YZm_2 + Z^2m_3)}{R^5} - \frac{m_3}{R^3}. \tag{B-17}$$

With accompanied magnetic moment derivatives as,

$$\frac{\partial B_z}{\partial m_1} = \frac{3 \cdot XZ}{R^5}, \tag{B-18}$$

$$\frac{\partial B_y}{\partial m_2} = \frac{3 \cdot YZ}{R^5}, \tag{B-19}$$

$$\frac{\partial B_y}{\partial m_3} = \frac{3 \cdot Z^2}{R^5} - \frac{1}{R^3}. \tag{B-20}$$

And lastly the derivatives of B_z with respect to the centre location,

$$\frac{\partial B_z}{\partial x_0} = \frac{15X \cdot (XZm_1 + YZm_2 + Z^2m_3)}{R^7} - \frac{3 \cdot (Xm_3 + Zm_1)}{R^5}, \tag{B-21}$$

$$\frac{\partial B_z}{\partial y_0} = \frac{15Y \cdot (XZm_1 + YZm_2 + Z^2m_3)}{R^7} - \frac{3 \cdot (Ym_3 + Zm_2)}{R^5}. \tag{B-22}$$

$$\frac{\partial B_z}{\partial z_0} = \frac{15Z^2 \cdot (Xm_1 + Ym_2 + Zm_3)}{R^7} - \frac{3 \cdot (Xm_1 + Ym_2 + 3Zm_3))}{R^5}, \tag{B-23}$$

B-4 Derivatives of TMI

The derivatives of the TMI work a little bit different then the ones for B_x, B_y and B_z. We now start off with the equation 2-37,

$$TMI = \sqrt{(B_{xa} + B_{x0})^2 + (B_{ya} + B_{y0})^2 + (B_{za} + B_{z0})^2} - \sqrt{B_{x0}^2 + B_{y0}^2 + B_{z0}^2}. \tag{B-24}$$

Although it looks a lot more complex, we can simply approach each vector component as its own function. Let's say $B_x + B_{x0} = f(x)$, $B_y + B_{y0} = g(x)$ and $B_z + B_{z0} = h(x)$, we can simply apply the chain rule to get a generalized derivative of the form,

$$\frac{\partial(TMI)}{\partial x} = \frac{f(x)\frac{\partial f(x)}{\partial x} + g(x)\frac{\partial g(x)}{\partial x} + h(x)\frac{\partial h(x)}{\partial x}}{\sqrt{f(x)^2 + g(x)^2 + h(x)^2}} \tag{B-25}$$

Equation B-25 can be used to calculate all six derivatives for the unknowns. The nice part is that we already have derived each derivative needed, since we already calculated all derivatives for B_x, B_y and B_z.

Since B-25 is the same everywhere and only the derivatives used in it are changed, it is unnecessary tow rite it out completely. Transforming $f(x), g(x)$ and $h(x)$ back to their original form leads to and notice that the derivative of B_{x0}, B_{y0} and B_{z0} is always zero, therefore we can simplify to

$$\frac{\partial(TMI)}{\partial x_j} = \frac{(B_x + B_{x0})\frac{\partial B_x}{\partial x_j} + (B_y + B_{y0})\frac{\partial B_y}{\partial x_j} + (B_z + B_{z0})\frac{\partial B_z}{\partial x_j}}{\sqrt{(B_x + B_{x0})^2 + (B_y + B_{y0})^2 + (B_z + B_{z0})^2}} \tag{B-26}$$

where $x_j = [m_1, m_2, m_3; x_0, y_0, z_0]$.